Alma Mater Studiorum - Università di Bologna

SCUOLA DI SCIENZE

Dipartimento di Chimica Industriale "Toso Montanari"

Corso di Laurea Magistrale in

Advanced Spectroscopy in Chemistry

Classe LM-71 - Scienze e Tecnologie della Chimica Industriale

Characterization and electrochemical study of a Prussian blue Analogue: Titanium Hexacyanoferrate

Tesi di laurea sperimentale

CANDIDATO

Cameron Sean Menzies

RELATORE

Chiar.mo Prof. Marco Giorgetti

CORRELATORE

Dott. Angelo Mullaliu

Anno Accademico 2016-2017

Abstract

Rechargeable batteries play an important role in portable consumer devices. Formulation of such batteries improved by researching new materials with higher performances of cyclability and negligible loss of efficiency throughout cycling. The goal of this work was to investigate a porous electrodic material, titanium hexacyanoferrate, and characterize it through a variety of analytical techniques. Synthesis was carried out by dropwise precipitation method, and characterization employed the use of techniques such as TGA, XRD, and ICP-OES. Electrochemical tests were performed both in glass and coin cells. Cyclic voltammetry was used in order to explore the electrochemical properties of titanium hexacyanoferrate in aqueous solutions, all while selecting for optimal conditions. With the use of Na^+ and K^+ salts, the studied material exhibited reversible processes and relatively high capacities. Coin cells were used to analyze the behavior of the material under galvanostatic cycling. The material displayed cathodic characteristics yielding a specific capacity of 35mAh/g at high potential, paving the way for future study on high power batteries.

Contents

List of Figures

List of Tables

1 Goals of this work

The main goal of this work is to study a series of reactions for an intercalation compound, $TiFe(CN)_6$, in order to determine the characteristics of the material, such as potential profiles, rate capabilities, and cycle lifetime.

The objectives of the work are as follows:

- To develop an intercalation material to be used as an anode.
- Characterization of the material through different analytical techniques such as XRD, ICP-OES, IR, and TGA.
- To make use of the cyclic voltammetry electroanalytical method to study the electrochemical properties of the material in different aqueous electrolytes, and in doing so select for optimal experimental conditions.
- To perform charge/discharge cycles on the synthesized material in organic electrolyte using coin cell geometry.

2 Introduction

High-efficiency electrochemical energy storage devices have become high in demand over the past few decades due to the rapid increase of global energy consumption and the drain of fossil fuels. A need to provide greater flexibility and stability is required in order to cope with this increase in demand, and to alleviate the impending crisis. The utilization of various sources of renewable energy such as solar, wind, and hydro, are limited by weather, storage capabilities, and must compete with conventional sources on a cost basis. Therefore, it is important to develop an energy storage system which can integrate effectively and smoothly. A crucial distinction has to be made between primary and secondary cells: a primary cell is able to harness the energy of a electrochemical reaction, during which the reactants are consumed in a single discharge process. A secondary or rechargeable cell may provide less energy and last for a shorter time period, however

it is able to provide several cycles of discharge/charge. Secondary batteries are one of the more promising means for storing electricity on a large scale due to their flexibility and high energy conversion efficiency, finding a wide market for portable consumer devices. [1, 2].

Lithium ion batteries (LIBs) are one such kind of secondary battery and are widely used due to their high energy density, high conversion efficiency, and long life cycle. A Ragone plot, as

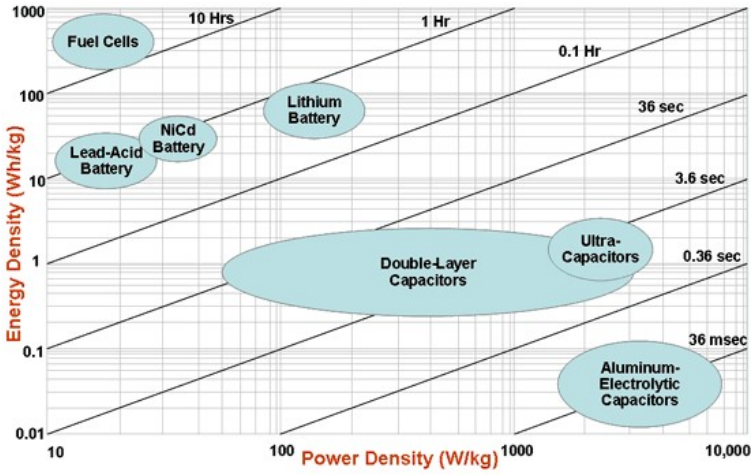

Figure 1: Ragone plot showing energy storage devices and how they compare.

seen in Figure1, is useful in demonstrating the different types of storage devices, and shows how they compare in energy storage. Fuel cells are located at top-left as they have relatively high energy densities and low power densities. while capacitors are at the bottom-right. A desirable energy device has both high energy and power density, which would be located at top-right. This is a straightforward way to judge an energy device by the location on the plot. In fact, any point on the graph lies on an iso-curve characterized by the slope Y/X, that represents the time required for delivering an amount of energy Y at a given power X. Energy density and Power density are defined as follows:

$$\text{EnergyDensity} = \frac{V * I * t}{m}, \ \text{PowerDensity} = \frac{V * I}{m} \tag{1}$$

where V is the voltage, I the current, t the time, and m the mass. According to the Ragone plot, LIBs have both greater energy and power densities compared to the lead-acid and nickel-cadmium batteries, lying on the same isocurve.

Lithium secondary cells consist of lithium metal as negative electrode, an active material (AM) as a positive electrode, and a non-aqueous lithium-ion containing solution which enables

ion transfer between electrodes. The electrode material should undergo a reversible reaction with lithium ions, a reduction upon discharge, and an oxidization when charged.

$$\mathrm{xLi^+ + AM(s) + } xe^- \underset{charge}{\overset{discharge}{\rightleftharpoons}} \mathrm{Li_xAM(s)} \tag{2}$$

Active material electrodes may have a porous framework that allows the rapid insertion and extraction of lithium ions with generally little lattice strain. *LixAM*s can be opted as negative electrodes, where the AM would act as a lithium ion sink, so the Li-ions would intercalate into both electrodes in an alternating fashion:

$$\mathrm{Li_xAM'(s) + AM(s)} \underset{charge}{\overset{discharge}{\rightleftharpoons}} \mathrm{Li_xAM(s) + AM'(s)} \tag{3}$$

This is more specifically known as the *rocking chair philosophy*[3].

Commercial *swing* batteries consist of graphitic carbon as a negative electrode and lithium cobalt dioxide as a cathode. During discharge, lithium is reversibly intercalated in the host material and electrons are able to flow through the external circuit to balance the reaction. Throughout charge, the non-aqueous electrolyte is able to mediate the transfer of Li-ions in the opposite direction. The conventional swing battery is depicted in Figure2.

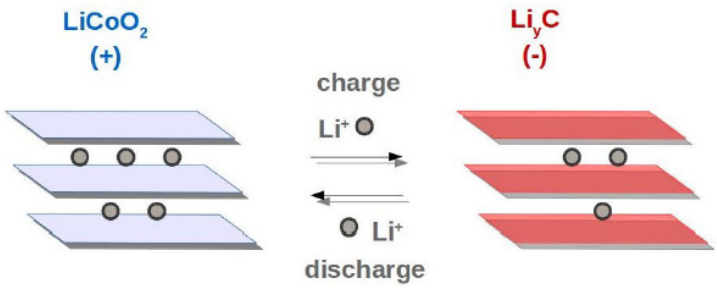

Figure 2: Graphic demonstrating the mechanics of the conventional *swing* battery.

LIBs can be found in electric vehicles, mobile phones, digital cameras, pacemakers, etc., and although highly popular the overall costs of lithium is one point that should be given more consideration from a consumption point of view. The price of lithium has been steadily increasing without pause over the past decade, much of the growth due to increased use in lithium battery

consumer electronics and large-scale energy storage projects. It is crucial to research alternative and affordable secondary batteries. Therefore, researchers have begun to focus on other alkaline, alkaline earth, and transition metal based rechargeable batteries [4, 5, 6, 7].

A possible solution for overcoming the disadvantages of LIBs would be the development of non-lithium batteries based on alternative metal ions such as Na^+ and K^+, or multivalent cations such as Mg^{2+}, Ca^{2+}, Zn^{2+}, Ni^{2+}, Al^{3+}, etc. Monovalent alkali metal ions such as Na^+ and K^+ have the advantages of being both high in abundance and low in price [8]. Multivalent ions have the added ability to transfer more than one electron at a time and would thereby be able to facilitate more energy storage than the aforementioned univalent cations. For instance, Mg^{2+} carries two charges per ion while maintaining an ionic radius as small as that of a Li^+, therefore the charge storage capability is doubled for the same cation volumetric concentration [9, 10]. Multivalent cations could possibly be more advantageous due to their theoretically higher energy density, yet the development of multivalent battery systems seems to be hindered by a lack of suitable chemistries that show high reversibility of ion intercalation. In either case, if the ionic radius differs than that of Lithium, the kinetic diffusion and storage mechanisms will differ. This may result in mechanical degradation in the anode materials, ultimately leading to poor life cycles [5]. It is crucial to find an electrode material with superior energy density, and one which is able to enhance electrochemical properties through controlling morphology, structure, particle size, and the formation of composites and compounds.

Prussian blue analogues (PBAs), which possess an open-framework crystal structure, have been closely investigated due to their structure and unique electrochemical properties. PBAs have a general formula of $A_xP[R(CN)_6]_\gamma \cdot v_{1-\gamma} \cdot nH_2O$, where A: alkali cations; P and R: transition metal; v: $[R(CN)_6]$ vacancy, as shown in Figure3. The open framework of the cyanoferrate (R=Fe) cubic lattice enables rapid solid-state diffusion of various monovalent and multivalent ions. The electrochemical properties of PBAs can be attributed to the redox behavior of the specific transition metal ions. The cyano ligands bound to the metallic centers link different metal centers together and may also add to the flexibility of the overall structure as a result of their stretching.

The Prussian blue analogue hexacyanoferrate (HCF) can exist in water as *soluble* or *insoluble* form, containing a $[Fe(CN)_6]^{3-}$ $F\bar{4}3m$ face-centered cubic and a $[Fe(CN)_5]^{2-}$ $Pm\bar{3}m$ cubic structure components, respectively. In the case of insoluble structure, water molecules may replace

the empty nitrogen positions in order to complete the coordination of the metal centered ion.

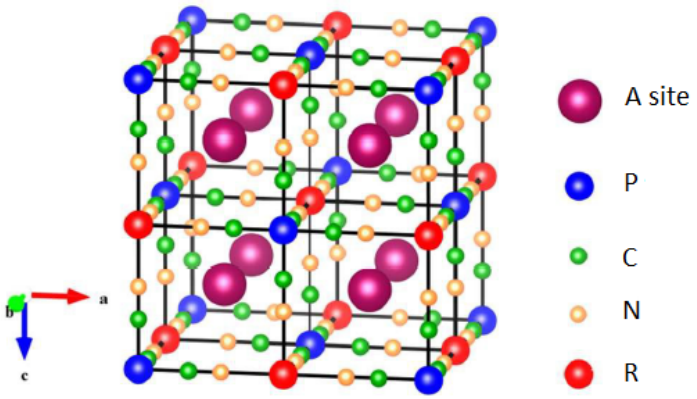

Figure 3: Schematic Diagram of the Unit Cell of the open framework of Prussian Blue Analogue Materials [12].

PBAs have been reported as electrode materials with good life cycles and rate performances in both aqueous and organic electrolytes. The open-framework structure enables high structural integrity with the possibility of accommodating multiple ions, thus leading to both fast kinetics and high capacity [8, 11]. The electrochemical activities of PBAs and its analogues were investigated as cathode materials for mainly sodium-ion batteries several years ago, such as $FeFe(CN)_6$, $NaFeFe(CN)_6$, $NaMnFe(CN)_6$, $NaMnMn(CN)_6$, etc. [13], which show reversible intercalation of lithium ions. Nevertheless, such PB-analogues has never been investigated as an anode material due probably to its relatively high working potential.

The Literature review will begin by introducing some of the observed phenomena which occur in electrochemistry, and current electroanalytical techniques will be shortly outlined along with many of the associated adjustable parameters. Following the introduction of electroanalytical chemistry, modern intercalation battery materials will be discussed along with the associated challenges for materials currently being studied.

3 Technical Background and Literature Review

3.1 Electroanalytical Chemistry

3.1.1 Electrochemistry and Double Layer Interface

Dynamic electrochemistry is the study of electron transfer reactions between electrodes and an electrolyte, or an ionic species in solution. Therefore, the study of the interaction between electrical energy and chemical change. In general, if an aqueous, heterogeneous electron transfer is considered, then the reaction follows the following form:

$$\mathrm{O}_{(\mathrm{aq})} + ne^- \underset{k_c}{\overset{k_a}{\rightleftharpoons}} \mathrm{R}_{(\mathrm{aq})} \tag{4}$$

Where O symbolizes the oxidized species, R the reduced species, and n is the number of electrons being transfered between the two. k_c and k_a are the respective reduction and oxidation rate constants. If k_c and k_a are so fast the the electrolysis is effectively in equilibrium, the concentrations of O and R at the electrode surface can be given by the Nernst equation:

$$\frac{[O]_{surface}}{[R]_{surface}} = \exp\left[\frac{nF}{RT}(E - E^0)\right] \tag{5}$$

where E^0 is the formal electrode potential when all species have unit concentration. This relates to the standard electrode potential via inclusion of activity coefficient effect. R is the ideal gas constant, T is the absolute temperature, F is Faraday's constant, and n is the number of electrons participating in the given reaction per mole of analyte. The process of redox reaction follows Faraday's Law in which the quantity of reacted species is directly proportional to the amount of current passing through the cell [14, 15].

The *Interfacial Region* is the region between the electrode and solution, where the reactions generally occur and where the greatest potential differences in the circuit appear. Throughout electrochemical experiments, a potential difference is applied between an electrode and a solution containing an electrolyte, and this applied potential leads to breakdown in the electrochemistry

of the solution close to the electrode surface. Figure4 demonstrates the electrical double layer model, depicting the diffusion layer, Inner Helmholtz plane (IHP), and the Outer Helmholtz Plane (OHP).

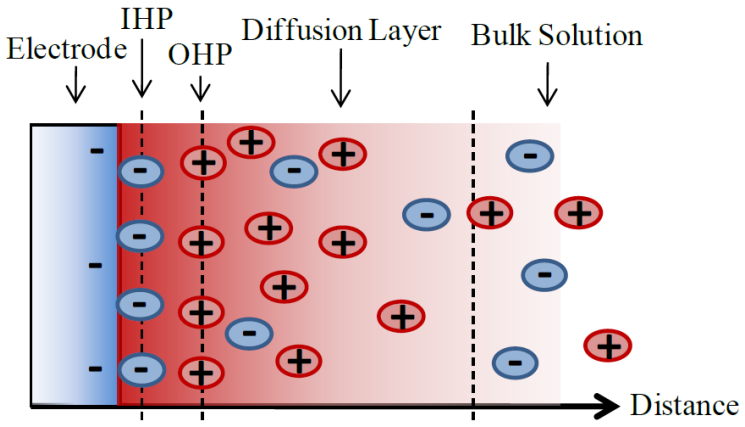

Figure 4: The electric double layer model [16].

In the double layer, solvated ions arrange themselves along the electrode surface forming a sheet of ionic charge called the Outer Helmholtz Plane (OHP) which is approximately 1nm from the electrode surface. At high enough voltages, the ions can also discard their solvation shell and adsorb onto the electrode surface forming an Inner Outer Helmholtz Plane (IHP). Ions on the surface shield the surface charge of the electrode, and remaining counter-ions have the tendency to diffuse away due to electrostatic interactions. The concentration of ions in the diffusion layer decreases with distance form the surface.

Electron transfer occurs over distances no greater than the OHP, therefore it is the potential drop across the double layer which influence the redox process. The rate of reaction depends on the slowest step of the process, generally mass transport, which in turn relies on three terms: diffusion, convection, and migration.

Diffusion occurs in all solutions where there is a concentration gradient, as entropic forces act to even out the uneven distribution of ions. Diffusion is the main driving force in the electrolysis process since the reaction occurs only at the electrode surface; it leads to a rise in concentration at the interface. Convection is generated by a thermal or density gradient and acts to mix the solution in a random way, and the concentration at a given location can change due to flow of the solution. It is possible to drown out the natural convection effects from an electrochemical

experiment by deliberately introducing convection into the cell. This form of convection is termed forced convection, and is generally used when the solution is pumped through the cell. Migration is essentially an electrostatic effect. When a potential is applied, the interface becomes charged and any charged species near that interface will be either attracted or repelled by electrostatic forces. However, due to ion solvation and the presence of a diffuse layer in solution, the migration is very difficult to determine.

Ultimately, the rate of mass transport can be described by the Nernst-Planck equation:

$$J(x,t) = -D\frac{\partial C(x,t)}{\partial x} - \frac{zFDC_\infty}{RT}\frac{\partial \theta(x,t)}{\partial x} + C(x,t)V(x,t) \tag{6}$$

where the three terms correspond to diffusion, migration, and convection, respectively. D is the diffusion coefficient, R is the ideal gas constant, T is temperature, C is the concentration of reagent, V is the velocity of the solution, $\frac{\partial \theta(x,t)}{\partial x}$ is the potential gradient in solution, and $\frac{\partial C(x,t)}{\partial x}$ is the concentration gradient. In order to simplify analysis, the solution is kept unstirred to render migration and convection negligible. The kinetics of the reaction can therefore be reduced to Fick's first law

$$J(x,t) = -D\frac{\partial C(x,t)}{\partial x} \tag{7}$$

When the reaction is mass transport limited, the rate of reaction, v, is governed entirely by the flux, J, at which the reagent is brought to the surface from the bulk solution:

$$J(x,t) = -\frac{i}{zFA} \tag{8}$$

where i is the current, z is the number of electrons involved in the reaction. Combining equations 7 and 8, the resulting current from redox can be expressed as a function of the concentration gradient: [17]

$$i = zFAD\frac{\partial C(x,t)}{\partial x} \tag{9}$$

Quantitative and qualitative analysis can be performed in the following two ways, poten-

tiometry or voltammetry. In potentiometry, no external potential is applied and no current flow occurs. The measured voltage results from the difference in free Gibbs energy of the electrons in equilibrium between the two half-cells. This difference is the redox potential difference. Potentiometry consists of 2 electrodes, the working electrode and the reference electrode. Voltammetry consists of applying a controlled external potential to the cell and measuring the resulting current, which can be done in one of two ways, via a potential sweep technique or a pulse techniques. Potential sweep involves applying a potential that is scanned linearly, while the pulse technique potential is increased in small increments. In either case, the set up is composed of 3 electrodes; the working electrode, the reference electrode, and the counter electrode. The two electrode potentiometry system can be used in the case of measuring very small currents that do not perturb the potential of the reference electrode [18].

3.1.2 Electrode Cell

The potential applied to the working electrode is controlled with respect to the reference electrode, as depicted in Figure 5. The redox reaction takes place at the surface of the working electrode and the current passes between the working electrode and the counter electrode. The counter electrode is convenient as its electrochemical properties do not affect the behavior of the electrodes of interest, the working or reference electrodes.

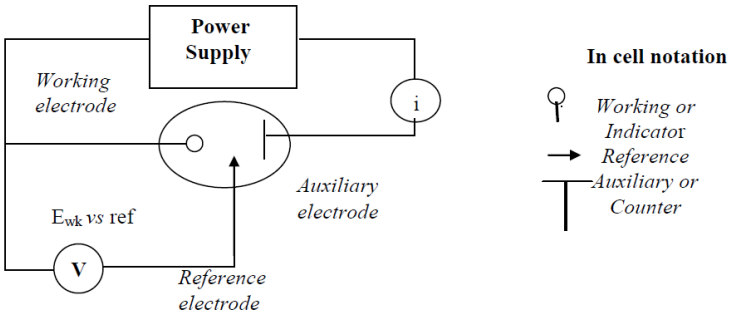

Figure 5: Three electrode cell and associated nomenclature [16].

The potential of the working-counter electrode system must be measured against a reference electrode, from which a well known potential can eventually be subtracted to have access to the analyte potential. Therefore the reference electrode must have a constant potential no matter the

species used or the concentrations. The most commonly used reference electrodes are the Standard Hydrogen Electrode (SHE), the silver/silver chloride electrode, and the Standard Calomel Electrode (SCE). Pseudo-reference electrodes may also be used.

Under standard conditions the Standard Hydrogen Electrode potential is zero. Figure6 demonstrates the platinum catalyzed reaction. As the hydrogen gas flows over the porous platinum, an equilibrium is set up between hydrogen molecules and hydrogen ions in solution. and the reaction

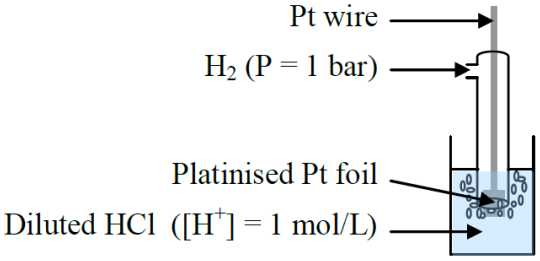

Figure 6: Standard Hydrogen Electrode [16].

proceeds as follows:

$$2H^+_{(aq)} + 2e^- \rightleftharpoons H_{2(g)} \tag{10}$$

The silver-silver chloride electrode consists of a silver wire coated with silver chloride, which is immersed in a saturated potassium chloride solution. A porous frit is used for the junction between the reference electrode solution and the sample solution. The redox process for this electrode is as follows:

$$AgCl_{(aq)} + 2e^- \rightleftharpoons Ag_{(s)} + Cl^-_{aq} \qquad E^0 = 0.22 \text{Vvs.SHE} \tag{11}$$

The Calomel electrode (SCE) is comparable to the silver/silver chloride electrode, with mercury replacing the silver:

$$Hg_2Cl_{2(s)} + 2e^- \rightleftharpoons 2Hg_{(aq)} + 2Cl^-_{aq} \qquad E^0 = 0.244 \text{Vvs.SHE} \tag{12}$$

Instead of the references electrodes described earlier, pseudo-reference electrodes can be used. They consist of simple metal wires (e.g., platinum or silver) having good inoxidizable prop-

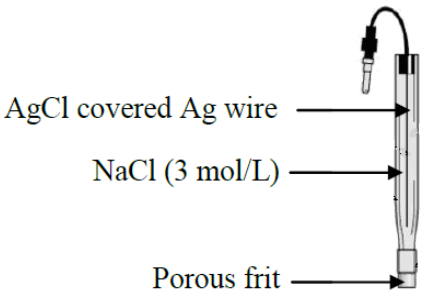

Figure 7: Silver-silver chloride reference electrode [16].

erties when directly immersed in the sample solution. Although the pseudoreference potential is unknown, and is dependent on the composition of the sample solution, these electrodes provide a stable reference potential when the samples under analysis are made of the same chemicals. Consequently, redox potentials measured using a pseudo-reference electrode should be quoted relative to the redox potential of the used reference compound. The main advantages of pseudo-reference electrodes are their low impedance and their ease of use.

3.1.3 Cyclic Voltammetry

Cyclic voltammetry (CV) is a very important electrochemical technique as it can be used to study the redox behavior of specific compounds and probe coupled chemical reactions in order to determine reaction mechanisms and rates of redox reactions. It is a simple extension of the linear sweep technique. Conventional (dc) cyclic voltammetry probably is the most widely used potential wave perturbative method for studying electrode processes. The use of a triangular waveform at stationary electrodes, allows both the oxidation and reduction pathways to be studied conveniently from the experiment, and quantitative theory has been extensively developed in a readily implemented form. Difficulties in CV include the ability to correct the charging current at high scan rates, performing data analysis on asymmetric peak-shaped curves, and determining the mechanism of secondary charge transfer reactions [19].

Figure8 demonstrates the potential dependence versus time throughout a linear sweep CV scan. λ is the value of time when the potential is reversed, and E_{min} is the minimum potential while E_{max} is the maximum potential. In cases where the electrode kinetics occur much faster

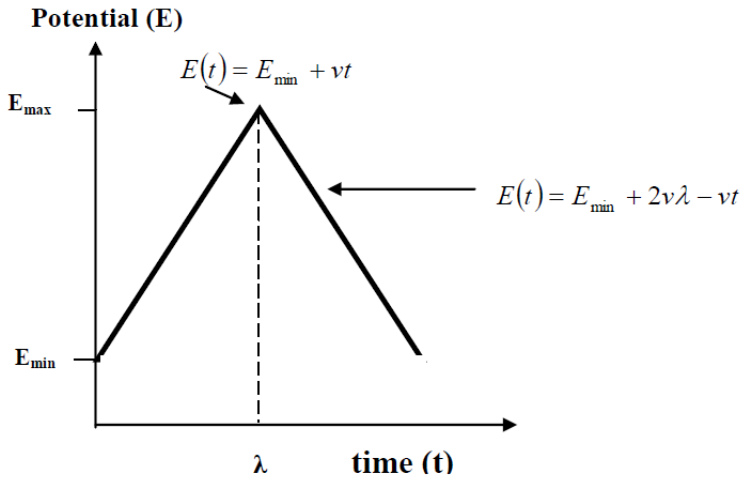

Figure 8: Potential Dependence on time throughout CV experiment [16].

than the rate of diffusion, the system is said to be reversible. Figure9 demonstrates the CV of a reversible system. The ratio of the peak currents at the anode (I_{pa}) and at the cathode (I_{pc}) can

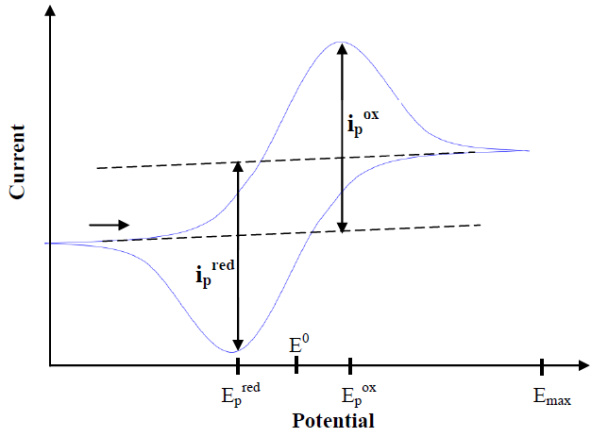

Figure 9: Illustration of a reversible system. The right-pointing arrowhead demonstrates the initial direction of scanning potential [16].

be set to equal 1, and the peak currents are said to be proportional to the square root of the scan rate as expressed by the Randles-Sevcik equation:

$$I_{pa} = 2.69 \times 10^5 z^{\frac{3}{2}} CAD^{\frac{1}{2}} \nu^{\frac{1}{2}} \tag{13}$$

where I_{pa} is the anodic peak current, z is the number of electrons involved in the reaction, C is the bulk concentration, A is the electrode surface area, ν is the scan rate, and D is the diffusion coefficient.

The size of the diffusion layer at the electrode surface will be different depending on the voltage scan rate. In a slow voltage scan, the diffusion layer will grow much further from the electrode in comparison to a fast scan. Consequently, the flux to the electrode surface is considerably smaller at slow scan rates than it is at faster ones. As the current is proportional to the flux towards the electrode, the magnitude of the current will be lower at slow scan rates than at higher scan rates. The influence of the voltage scan rate on the current for a reversible electron transfer is illustrated in Figure10.

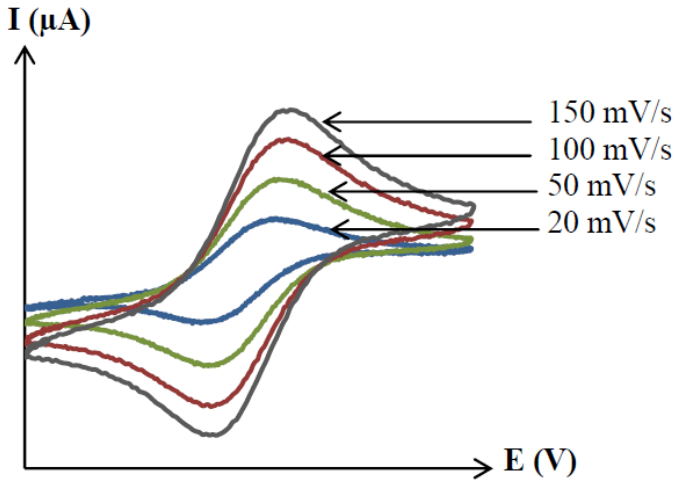

Figure 10: Graphic representation of the influence of voltage scan rate on the current response for a cyclic voltammetry cycle [16].

In CV analysis, the supporting electrolyte is a non-reactive ion that behaves as an electrically conductive medium. It is present in high concentration in comparison with the reactive species in order to minimize the resistance of the solution and to prevent charged species migration. The potential window of the analysis is defined as the potential range in which an electrode can be polarized in a solution without the passage of current. As shown in Figure11, current may arise due to the the oxidation or reduction of the supporting electrolyte. The choice of potential window depends on the nature of the solvent, the nature of the electrolyte, the nature of the electrode material, and on the presence of possible contaminants. The more resistant the electrolytes ions are to reduction an oxidation, the wider the potential window may be [20].

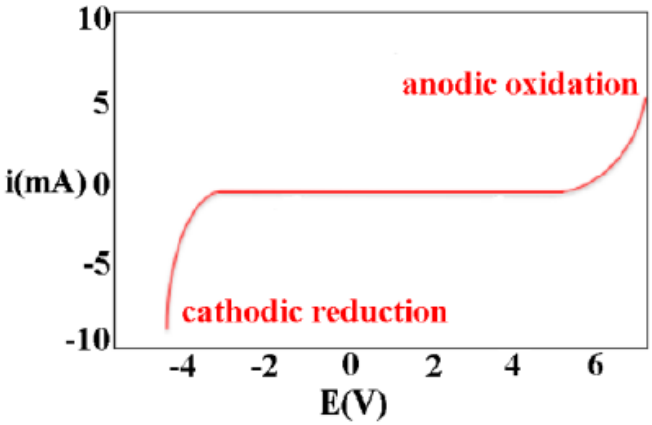

Figure 11: CV voltammogram of an electrolyte being oxidized and reduced within the given potential window [16].

3.2 Electrolytes and Multivalent Intercalation

There has been a large development in the research conducted on multivalent battery systems in aqueous electrolytes, however when analyzing a specific material it can be difficult to decide on which electrolytes to use. Therefore it may be helpful to review some already successful systems and the associated challenges in order to act as a guide when deciding which salts should be used for a specific material.

HCFs have been investigated as cathode materials in many sodium-ion batteries, but have not been widely studied as an anode material due to its relatively high working potential. However, it has been reported by using a simple solution of introducing a Ti^{4+}/Ti^{3+} redox couple, a $TiFe(CN)_6 \cdot 2H_2O$ material can be synthesized and can be used as an anode as it possesses relatively low potentials when used with lithium or sodium-ion batteries[13].

The multivalent cation chemistries are principally advantageous for their energy density and improved safety. In fact, many of these multivalent ions are light enough to deliver high energy densities compared to the Li-ion batteries. Table1 shows a comparison of different multivalent metal anodes in terms of their standard electrode potentials, and specific and volumetric capacities with reference to Li^+ and the widely studied Na^+ anodes [5].

Table 1: Standard Electrode Potentials and Theoretical Capacities of Univalent and Multivalent Anodes. Capacities are recorded as Theoretical Values [8]

Ion	Standard Electrode Potential (V)	Specific Capacity (mAh/g)	Volumetric Capacity (mAh/cm^3)
Li^+	-3.05	3829	2044
Na^+	-2.71	1165	1128
K^+	-2.93	685	591
Mg^{2+}	-2.36	2234	3881
Zn^{2+}	-2.20	820	5854
Al_{3+}	-1.66	2980	8046

3.2.1 Solvent

Dahn *et al.* used aqueous electrolytes for Li-ion batteries, leading to a large following of groups willing to do research using aqueous solvents [21]. Intercalation reactions are usually very complicated in aqueous electrolytes. There could be different side reactions such as the co-intercalation of protons into the electrode materials along with the intercalation of multivalent ions, the reaction of electrode materials with water or oxygen, the evolution of hydrogen/oxygen, and the pH dependent dissolution of electrode materials in water. The proton co-intercalation could happen in the positive electrode materials, and it usually depends on the crystal structure of the electrodes and pH of the electrolyte as well.

3.2.2 Sodium

Sodium Ion Batteries (SIBs) are considered to be one of the most appealing alternative batteries to LIBs, with a theoretical capacity of $1165 mAhg^{-1}$ and a negative reduction potential of $-2.71V$ *vs* SCE. However, since the size of Na^+ is larger than Li^+ ($1.02\mathring{A}$ *vs* $0.76\mathring{A}$ for Li^+), Na^+ diffusion kinetics are generally slower and materials require relatively larger interstitial spacings in order permit the passage of Na^+ [8]. One practical limitation to the incorporation of Na-ion batteries is the low availability of adequate insertion materials, as graphitic carbons do not intercalate Na^+ and the irreversibility of both the insertion and extraction are more susceptible to alternative side reactions when compared to Li-ion batteries. [22].

3.2.3 Magnesium

Initial efforts done by Gregory and Novak *et al.* on multivalent Mg-ion batteries showed successful chemical and electrochemical insertion of Mg^{2+} into various transition metal oxides and sulfides [5, 23, 24]. Intercalation of Mg^{2+} into other materials such as V_2O_5 and MoO_3 was later performed, however there appeared to be a screening effect of water on Mg^{2+} cations during the process. V_2O_5 aerogels also showed proved to be a success, as the associated water molecules provided steric hindrance within the structure, aiding in reversibility. Mg^{2+} could also be used as an anode as dendritic growths on the interface was not observed. However promising Mg^{2+} proved to be, it remained restricted. The high charge density of Mg^{2+}-ions contribute to a large desolvation energy which would hinder the diffusion of cation in to the electrode at the interface.

3.2.4 Aluminum

Although Al^{3+} is smaller than Li^+ in the unsolvated state ($53.5pm$ *vs* $76pm$ of Li^+), due to its tri-valent nature Al^{3+} ions possess slower diffusion kinetics within certain electrodes. Therefore the successful intercalation of Al^{3+} is highly material dependent, such materials including anatase (TiO_2) and Copper Hexacyanoferrate ($CuHCF$). Although aluminum may seem as a promising candidate as electrolyte, it has been reported that aluminium cations are generally found in solvated complexes[25].

In 2012, Liu *et al.* for the first time demonstrated the storage capability of Al^{3+} in anatase TiO_2 nanotube arrays (NTAs) using $AlCl_3$ electrolyte [26]. The insertion of Al^{3+} into NTA resulted in the reduction of Ti^{4+} to Ti^{3+}/Ti^{2+}, but the reaction showed to be slightly irreversible as the extraction process was unable to oxidize Ti^{2+}. The reaction pair Ti^{4+}/Ti^{3+} aided in storing Al^{3+} in the NTAs, and a maximum discharge capacity of $75mAh/g$ was obtained with a redox couple at -1.26 and $-0.84V$ *vs* SCE. Liu *et al.* also studied the reaction upon the addition of $Al_2(SO_4)_3$ and $NaCl$ in different concentrations in order to see the effect of Cl^-. A discharge capacity of $74.8mAh/g$ was obtained at a current density of $4mA/cm^2$, and were able to attribute the high performance to the presence of Cl^- in the electrolyte. He *et al.* were also able to report a capacity of $278mAh/g$ at a current density of $0.05A/g$ using an $Al(NO_3)_3$ electrolyte [27].

Cui *et al.* were able to observe similar behavior in the open structured CuHCF, where the insertion of trivalent Al^{3+} was made possible without electrolyte decomposition and associated with a low hysteresis of charge-discharge curves [28]. Referring again to Figure3, the large interstitial A sites are where the insertion of ions occurs. CuHCF PBAs have the capacity to insert many ions, regardless of their valency, as they are characterized by their porous nature. The number of available Fe^{2+} ions in the crystal structure is what limits the cell capacity in this case, which has been shown by Steingart *et al.* in 2016 [29]. Using a $Al_2(SO_4)_3$ aqueous electrolyte and CuHCF as a cathode material, a specific capacity of $62.9mAh/g$ at a current density of $50mA/g$ and decreased to $46.9mAh/g$ at a current density of $400mA/g$, a retention of 74.6%.

3.2.5 Zinc

Zinc-ion intercalation batteries have gained popularity in hopes of replacing conventional Li-ion batteries for large scale applications, as they can be manufactured economically and the electrolytes possess simple chemistry [30].

Zn-ion intercalation in both α- and γ-MnO_2 compounds has shown to be successful. Reversible intercalation of Zn^{2+} into the tunnel structures of α-MnO_2 resulted in a capacity of $210mAh/g$, however they only possess a capacity retention for up to 30 cycles at a current rate of $C/20$. The loss in capacity was associated to the phase transition of α-MnO_2 Zn-birnessite. Intercalation of Zn^{2+} into γ-MnO_2 demonstrated a discharge capacity of $442.6mAh/g$, however at a current density of $408mA/g$, the capacity dropped to only $33.8mAh/g$ [31]. As early as 2013 Zn-ion intercalation into cuHCF had been investigated as well, yielding a reversibility of intercalation with a specific capacity of $56mAh/g$ [32]. Full insertion and extraction of Zn^{2+} in the CuHCF was attributed to the small steric effects of Zn^{2+} as it has a small ionic radius.

3.2.6 Potassium

In pursuit of alternative LIBs, nearest neighbour elements such as Na^+ and Mg^{2+} seem to have been a popular choice for the replacement Li^+ due to property similarities. In any case, the potential of potassium is similar to that of lithium (see Table1), and as a result Potassium

Ion Batteries (KIBs) are attracting interest. The first KIB prototype was introduced in 2004 by Eftekhari *et al.* utilizing a PB cathode [33]. Making use with a Prussian blue cathode material, a reversible capacity of $87.36mAh/g$ with a current density of $0.1mA/g$ was obtained, and possessed a high cyclability lasting over 500 cycles. The chemical diffusion coefficient of K^+ is reported higher than that of Li^+ as well. Nickel and Copper HCF reported sightly lower capacities of $59mAh/g$ and $60mAh/g$, respectively. Analogues of Prussian blue can provide many cyclic-voltammetry cycles in aqueous electrolyte, exhibiting high reversibility and long cycling life [34].

The electrolyte challenges are magnified for multivalent batteries, and their choice is very critical in terms of high ion mobility and desolvation of the ions at the electrode interfaces.

The common approaches to mitigating the interface and solid state diffusion issues of multivalent ions include "nano-sizing" of the electrode materials to shorten the diffusion distances, application of electrode materials with large tunnel structures or interlayer spacing, and partial shielding of the multivalent ions with polar molecules such as water. The electrodes with larger spacing will help minimize the steric hindrance effects. The nanostructures of electrodes will also reduce the impact of structural distortions during intercalation and de-intercalation of the multivalent ions.

$TiFe(CN)_6$ provides as a good candidate as the stretching of cyano ligands provide flexibility, the porous framework allows for the diffusion of many different ions, and the material is relatively easy to synthesize at low cost with high scalability.

4 Experimental Methods

4.1 Synthesis

The synthesis of $TiFe(CN)_6 \cdot 2H_2O$ was carried out via a solution precipitation method upon the introduction of a Ti^{3+}/Ti^{4+} redox couple. 50mL of a 0.1M tetrabutyl-titanate-ethanol solution was slowly added to 100mL of a 0.1 M $Na_4Fe(CN)_6$ aqueous solution containing 1.5 M HCl. The $Na_4Fe(CN)_6$-HCl solution is kept in a heat bath at 40°C and placed under continuous stirring set at 10rps to generate a precipitate. The tetrabutyl-titanate solution was added dropwise over the course of one hour, and done so under inert atmosphere (N_2) in order to avoid the spontaneous ignition of the solution, as its flashpoint is at 50°. Following dropwise addition, the solution was heated under N_2 with stirring for another 12 hours to ensure the completion of reaction. The resulting solution was dark in color, resembling black, however after centrifuging for 2 days a precipitate collected on the walls of the round bottom flask. This precipitate was found to demonstrate a hint of dark blue color. The product was washed and centrifuged multiple times with water and acetone, and then dried at 70° for another 12 hours. 1.305grams were obtained from the synthesis. This method proves to be simple and if desired, production could be scaled in the case of high demand. The yield was 42.09%.

4.2 Electrode Preparation

The electrochemical tests were done on polytetrafluoroethylene (PTFE) based electrodes, as shown in Table2

Table 2: Electrode composition.

Material	Composition $[mg]$
ActiveMaterial	70.21
CarbonBlack	10.04
PTFE	10.16
CarbonFibers	10.22

The electrodes were prepared so that they contained 70 wt-% of active material (AM),

10 wt-% carbon black (CB), 10 wt-% vapor grown carbon fibers (VGCF), and 10 wt-% PTFE. The AM, CB, and VGCF were ground in an agate mortar. PTFE was then added to the powder mixture, and mixed again in a mortar until a homogeneous paste was formed.

VGCF are nano-carbon fibers containing an exposed outer surface. CB and VGCF were added to enhance the electrical conductivity of the electrode while PTFE was added as a binder material. PTFE is used for its hydrophobic property as it is resistant to alkali solutions, and overall flooding of the electrode material is inhibited [35]. A prepared pellet is shown in Figure12, possessing a diameter of $0.8cm$ and an approximate weight of 10mg:

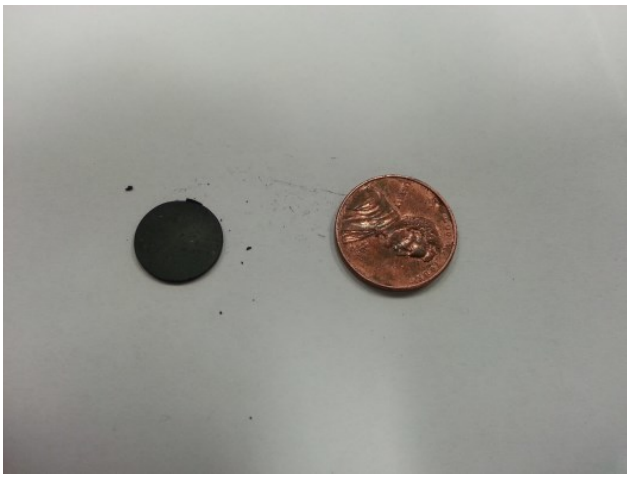

Figure 12: Preparation of electrodes using 70 wt-% active material combination. Diameter of pellets are $0.8cm$

The pellets are suspended in an Aluminum mesh, and mounted into a three electrode system in an electrochemical cell, as the current and potential need to be monitored.

5 Results

5.1 Characterization

5.1.1 X-Ray Diffraction - XRD

Powder X-ray diffraction (XRD) was performed in the range $10° \leq 2\theta \geq 70°$ using Cu K-alpha radiation ($\lambda = 1.5418\mathring{A}$). The profiles were refined with pseudo-Voigt peak shapes using Fullprof Suite software. Figure13 displays the powder XRD profile of the synthesized titanium hexacyanoferrate and its profile matching refinement. The residual curve is plotted to provide a quality check of the fitting performance. The material presents a high degree of crystallinity. After profile matching with constant scale factor, a space group of $Pm\overline{3}m$ resulted, hence a cubic structure characterized by the average cell parameter $a = 10.190(2)\mathring{A}$. XRD experiments were performed in Lille, France.

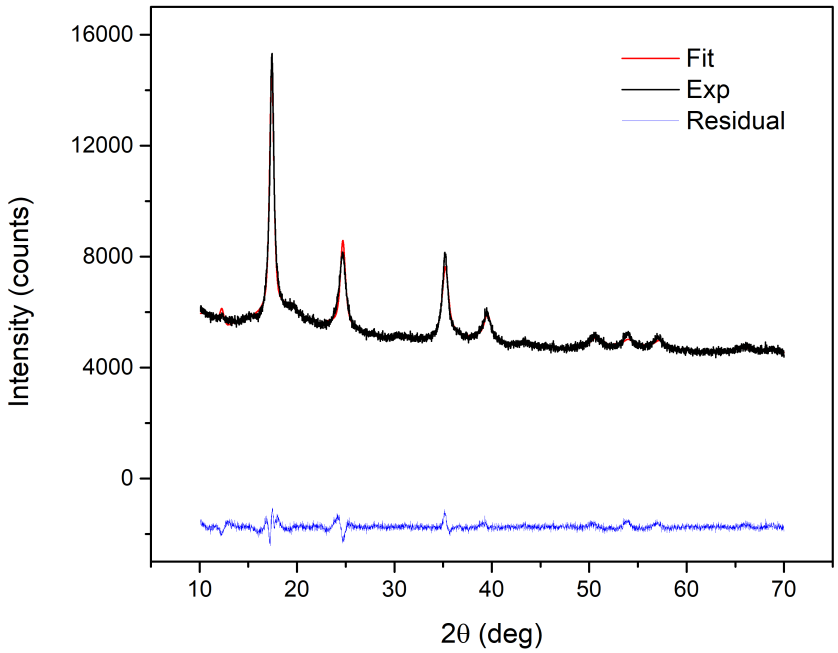

Figure 13: XRD pattern of titanium hexacyanoferrate and its profile matching refinement. The obtained space-group was $Pm\overline{3}m$, with a cell parameter of $a = 10.190(2)\mathring{A}$.

As host materials are able to insert ions in their channels and cavities, a peak shift in XRD diffractograms would be expected. The intercalation of ions generally results in an increase in the interplanar distance, resulting in a gradual peak shift towards smaller 2θ angles. Nevertheless, if attractive forces prevail over steric hindrance, the opposite is observed. In literature, it is common the appearance of new phases, which is demonstrated by the emergence of new peaks in the XRD pattern. For this reason, XRD profiles have been recorded on both pristine and cycled material in an attempt to observe multiple phases. X-ray diffraction (XRD) was performed in the range $10° \leq 2\theta \geq 70°$ using Cu K-alpha radiation ($\lambda = 1.5418\mathring{A}$) in Lille, France.

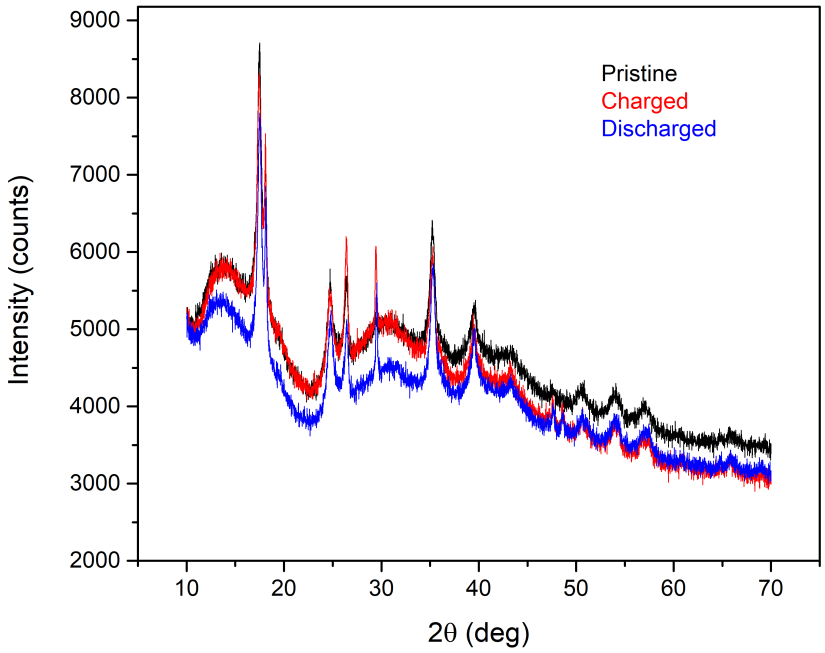

Figure 14: XRD profiles of the pristine titanium hexacyanoferrate, and the cycled electrodes in the discharged and charged states.

Table 3: Conditions pertaining to the pristine, charged, and discharged states of the XRD analyte. Potentials were selected with help from completed cyclic voltammograms in KNO_3.

Electrode	Applied Potential [V]	Time span [min]	Peak Centroid [θ]
Pristine	-	-	17.49
Charged	0.7	25	17.46
Discharged	-0.6	25	17.51

Patterns appear noisier than XRD done on powder due to the formulation and treatment,

therefore profile matching refinement is not as straightforward. Nevertheless, a few considerations: (i) no extra peak appears for charged and discharged electrodes with respect to the pristine material, so we can assume that during cycling in KNO3 aqueous medium no new phase is formed; (ii) reffering to Figure**??**, where a zoomed area of the patterns is pictured, the centroid of the main peak positioned at 17.5 degrees varies according to the state of charge of the electrode. This fact is related to interplanar distance, and even though we are not able to quantitatively assign cell parameters for formulated electrodes, we are still able to deduce a general trend. In fact, if we consider an ion-intercalation process that takes place during discharge, it can can be said that the presence of K-ions in the cavities results in a contraction of the lattice, according to the shift of the main peak towards greater values of 2θ. Conversely, the extraction of K-ions during oxidation produces an expansion and a shift towards smaller 2θ. In essence, the slight lattice strain is said to be caused by the insertion/extraction of potassium ions in the host material. The presence of cations in the interstices lowers cell dimensions as a response to attraction forces between K-ions and ions in the lattice.

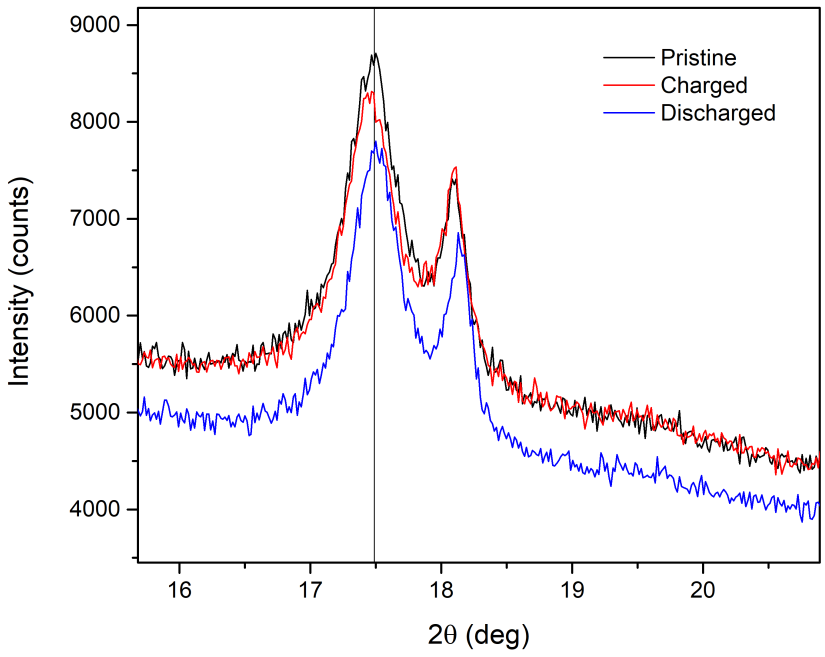

Figure 15: A section of the XRD profile for pristine titanium hexacyanoferrate, as well as the cycled electrodes in the discharged and charged states. The centroid has a slight shift in 2θ value depending on the state of charge of the material.

5.1.2 Thermogravimetric Analysis - TGA

In general, when hexacyanoferrate compounds containing water are heated, an endothermic effect (always below $200°C$) corresponds to a release of the water molecules. Afterward, the thermal decomposition occurs at higher temperatures depending on the composition of the starting compound. Decomposition in the presence of O_2 occurs with the formation of gaseous $(CN)_2$ or HCN, followed by the oxidation of iron cations forming iron oxides [36]. The thermal decomposition reactions under N_2 resulted in the formation of $Fe(CN)_2$, followed by further decomposition of to FeC, and finally to metallic iron. The structure of PB heated up to $450°C$ is partially destroyed, emitting gaseous cyanide groups, and formig crystalline ferrous ferrocyanide[37].

TG analysis was done under inert atmosphere (N_2) at a ramping rate of $10°C$/min. Temperature analysis ranged from $25°C$ to $500°C$ for the sample. Analysis of the off-gas was not completed due to equipment restrictions. Referring to Figure16, the curve in green represents the loss in weight percentage, while the blue curve represents the change in weight percentage with respect to temperature, or the derivative. The temperature at a peak would correspond to a maximum rate in change in weight%, or the temperature at which the material is said to be decomposed. There is a mass loss at three different temperature ranges, $110-150°C$, $250-325°C$, and $325-400°C$. The first mass-loss step $110-150°C$ is essentially entirely due to the loss of intrinsically adsorbed and interstitial water molecules. TG-MS studies have been performed on similar materials, such as $Fe[Fe(CN)_6]\cdot nH_2O$, and prior to $200°C$ there is only evidence of water evolution. This would dictate that the material is 10 wt-%, which will aid in chemical formula determination. The remaining decompositions at $250-325°C$ and $325-400°C$, typical for correspond to the decomposition of the material, perhaps attributed to the presence of *soluble* and *insoluble* configurations, differing on their tendency to form colloidal solutions due to the presence of interstitial cavities.

5.1.3 Atomic Emission Spectroscopy Optical Emission Spectroscopy - ICP-OES

A variety of methods are typically used to detect trace metals in a material, one of which being ICP-OES. This multi-element technique heats samples to a temperature of approximately $10,000°C$ to achieve effective excitation. The atoms in the sample then emit light at element-

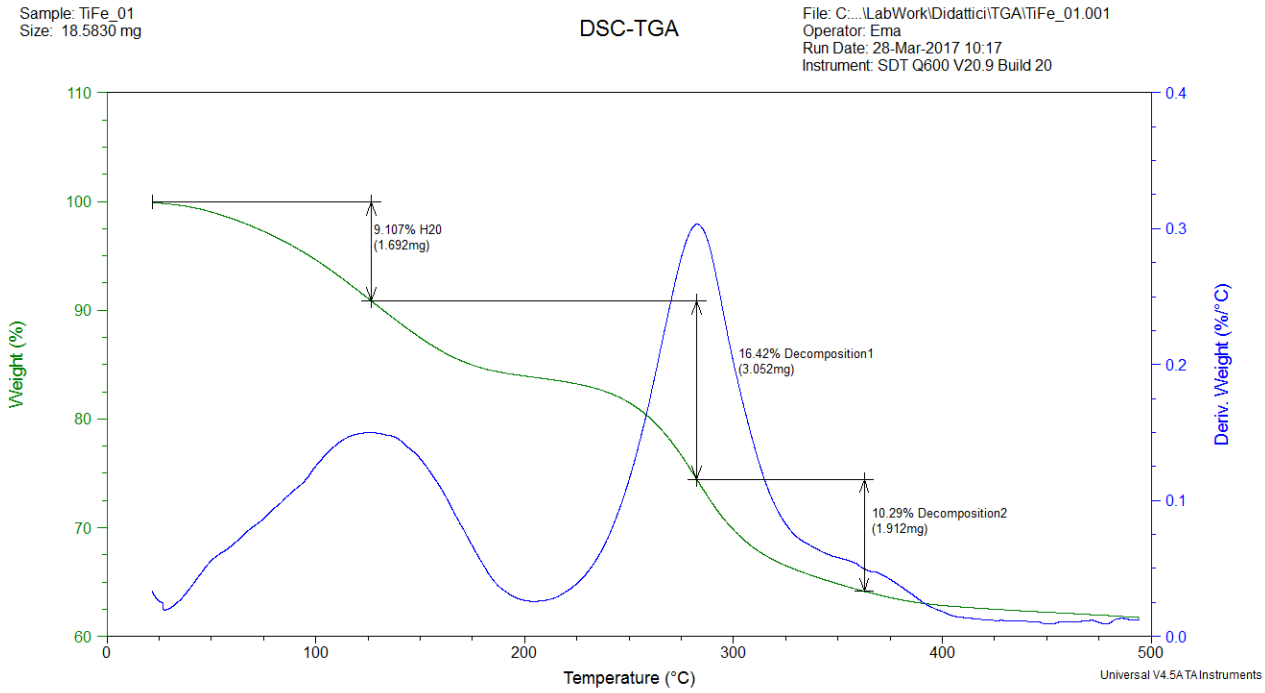

Figure 16: : TGA analysis of $TiFe(CN)_6$ sample. Curve in blue represents the change in weight percentage with respect to temperature. The temperature at a peak would therefore correspond to a maximum rate in change, or the temperature at which the material is decomposed.

specific wavelengths. The constituent elements can be identified by their characteristic emission lines, and quantified by the intensity of the same lines. ICP-OES was performed in Lille, France and results are summarized in Table4

Table 4: Metallic composition by ICP-OES on the active material $TiFe(CN)_6$.

	Iron	Titanium
Content wt-%	15	17

With the information provided by both TGA and ICP-OES, it is possible to determine the chemical formula of our active material, $TiFe(CN)_6 \cdot nH_2O$. Normalized to Iron, the compound has an ideal chemical formula of

$$Ti_{1.3}Fe(CN)_6 \cdot 1.8H_2O$$

.

5.1.4 Infrared Spectroscopy - IR

Infrared (IR) spectroscopy is a well-adapted probe of the electronic and structural properties of PBAs at the molecular level as it is possible to probe the electronic and structural properties of any material. Figure17 shows the spectrum obtained when analyzing $Ti_{1,3}Fe(CN)_6 \cdot 1.8H_2O$.

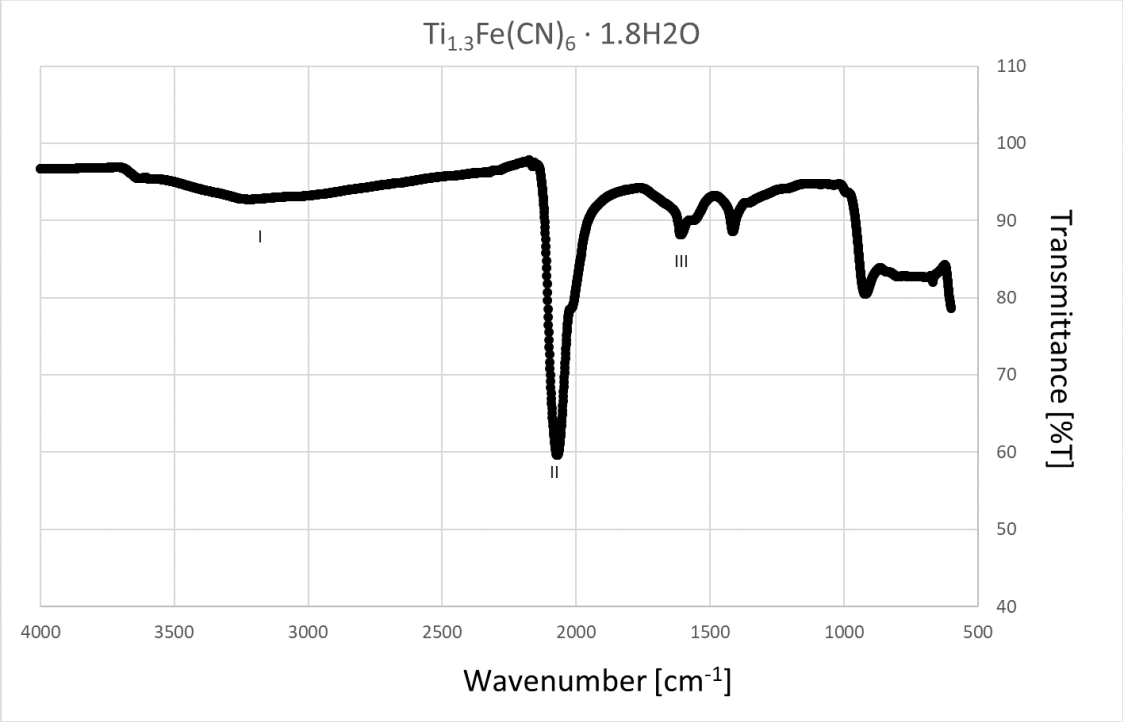

Figure 17: IR spectrum of $TiFe(CN)_6$. Two easily distinguishable peaks occur at $3250cm^{-1}$ and $2100cm^{-1}$. Peak I is due to OH hydroxyl group stretching in the sample, whereas peak II at 2100cm-1 is due to the stretching frequency of CN group, highly characteristic to HCF compounds. Peaks at 1600cm-1 may be associated with OH stretching.

According to the composition and the structure of the material, the IR spectrum is expected to exhibit v(C≡N) vibrations, related to cyanide bridges; v(Ti-N) and v(Fe-C) vibration bands related to the metal-to-ligand bonds which generally occur at lower energies; and a v(O≡H) corresponding to the water molecules, those which are bound to the metal cations at the $Fe(CN)_6$ vacancies. The vibration band is located in the $21002200cm^{-1}$ spectral range. As the cyanide bridge is extremely sensitive to its environment, including the oxidation state and the spin state of the metal cations involved, the v(C≡N) band has already been extensively used to characterize

Prussian blue analogues. In this case, the vibrational band occurs at $2100cm^{-1}$, and may be associated to $\mathrm{Ti}^{III} - \mathrm{N} \equiv \mathrm{C} - \mathrm{Fe}^{II}$. The small contributions located between 2000-2050 cm^{-1} may be due to $\mathrm{Ti}^{II} - \mathrm{N} \equiv \mathrm{C} - \mathrm{Fe}^{III}$, surface non-bridging cyanides, or $\mathrm{Ti}^{II} - \mathrm{N} \equiv \mathrm{C} - \mathrm{Fe}^{II}$ linkages. The spectral range associated with $v(\mathrm{O}{\equiv}\mathrm{H})$ displays two distinct regions: from 3000-3500cm^{-1}, the IR spectrum exhibits very broad bands associated with water molecules involved in a hydrogen-bonded network; and from 3550-3700cm^{-1}, the IR spectrum exhibits one or several very sharp bands associated with water molecules that are not involved in a hydrogen-bonded network and therefore interacting with metallic cations. The absorption peaks at $1610cm^{-1}$ are associated with the stretching mode of O-H arising from water coordination in the sample, as water may occupy $Fe(CN)_6$ vacancies [38].

5.2 Electrodes

Upon initial utilization of the newly prepared electrodes, many of the cyclic voltammograms returned unsuccesful. This is likely associated with the difficulties in performing cyclic voltammetry on pellets, rather than the commonly studied electrodeposits. Many, if not all, of the voltammograms returned with a poor lifetime and demonstrated very poor electrical contact, such as the one displayed in Figure18, provided unreliable outputs. Pellets are analyzed directly, rather than

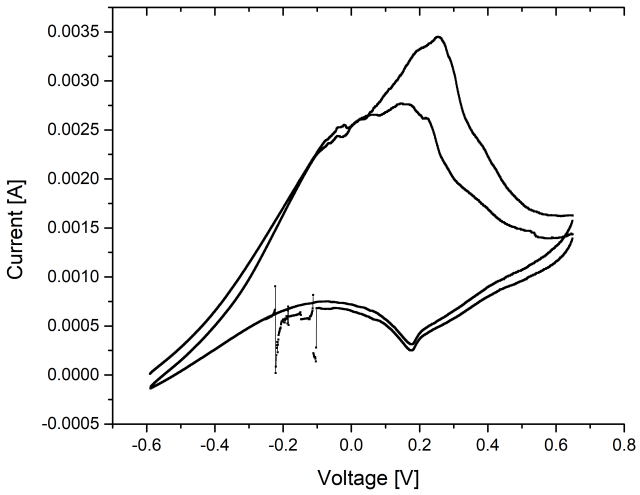

Figure 18: Cyclic Voltammagram of a 1M K_2SO_4 solution, performed at a scan rate of 1mV/s. Note the large interference occurring along the reduction sweep during the second cycle.

making use of the electrodeposition technique, as we desire to acquire electrochemical information about the formulated material to be used in future energy storage prototypes.

When unexpected results such as these occur, it may not be obvious as to what is the cause of the problem. The perturbation may be due to noise, current signal overload, potential overload, material dissolution, mesh disintegration or interference, bubble formation on the reference electrode, or perhaps contact problems in the circuit. Generally, noise occurs when there is not a sufficient electrical network, and secondary current can easily pass through and be recorded throughout the experiment. Upon inspection of the circuitry, it was noted that every experiment had a short lifetime as the metal clip supporting the electrode was corroding. Figure19 demonstrates the layout of a typical three-electrode cell. The aluminum mesh containing the active material is in

Figure 19: Set-up demonstrating the three-electrode cyclic voltammetry experiment. The three-electrodes cell from left to right: Working electrode containing the active material, SCE the Reference electrode, and a platinum counter electrode. Note the coating on the aluminum mesh at the clip joint.

contact with the electrolyte as well as the clip used in electrochemical analysis. In order to prevent the corrosion, it was necessary to inhibit the capillary action of the electrolyte in the aluminum mesh. Solder would usually provide as a useful solution in creating a conductive layer between the aluminum mesh and the clip, yet soldering aluminum has its difficulties. In order for soldering to be successful, the solder would need to melt on a surface and then flow into a joint, also by capillary action. Generally, this flow would occur along a temperature gradient from low to high temperature, due to what is known as the Marangoni Effect. The Marangoni effect takes place when there is a temperature gradient at the interface between two phases, in this case liquid solder

and solid aluminum. Aluminum possesses a large thermal conductivity, however, and heating up a local area to high temperatures can be difficult. The aluminum mesh would need to be exposed to heat over a longer period of time in order to facilitate the solder flow. This is problematic as heating aluminum to such high temperatures over an extended period of time, the formation of an aluminum oxide layer becomes more and more problematic.

An alternative solution would be to coat a section of the aluminum mesh in a conductive paint. The paint would occupy the space within the mesh, inhibiting the flow of electrolyte, but would still be able to facilitate the flow of electrons. Silver paint is one that would fill these requirements as silver contains one of the highest electrical conductivities of any metal. A successful coating can be seen in when referring to the working electrode in Figure19.

5.3 Cyclic Voltammetry - CV

Cyclic voltammetry was performed on the active material with a set of different electrolytes. These electrolytes varied both in cation and anion compositions, all in an attempt to explore the electrochemical activity of the electrode. Initially there were a set of variables that had to be optimized, such as potential window, electrolyte concentration, CV scan rate, and the mass loading. A multitude of experiments were performed in an effort to discover optimal conditions, and a variety are demonstrated in Table5. When not specified, potentials are referred in reference to the Calomel electrode, SCE.

Table 5: Data obtained from Cyclic Voltammetry. Information useful in determining the reversibility of the reaction based on current ratio as well as diffusion constant estimate. Sample CV diagrams are provided in the Appendix.

Salt	Concentration $[mol/L]$	Scan Rate $[mV/s]$	Current Ratio $\frac{I_a}{I_c}$	Potential Separation E_p $[mV]$
$NaNO_3$	0.01	1	0.131	816.07
	0.1	1	1.03	368.92
	1	1	0.549	481.96
Na_2SO_4	0.1	1	0.689	203.50
KNO_3	0.01	1	0.242	542.66
	0.1	1	0.900	178.185
	1	20	0.586	668.22
	1	10	0.676	480.21
	1	1	0.741	149.12
K_2SO_4	0.05	10	-	-
$Zn(NO_3)_2$	0.01	1	0.00775	358.27
	0.1	100	0.367	376.44
	0.1	10	0.239	198.03
	0.1	1	0.570, 1.953	156.58, 730.12*
AlN_3O_9	0.01	1	0.238	569.609
	0.1	20	0.377	594.84
	0.1	10	0.239	551.94
	0.1	1	0.793	459.91
$MgSO_4$	0.1	1	0.332	299.00
	0.1	20	0.568	672.77
KCl	0.01	1	-	-
NaCl	0.01	1	-	-
$LiClO_4$	0.1	1	-	-

The peak potential separation (E_p) and peak current ratio I_{pa}/I_{pc} are two variables capable of determining the efficiency of cation insertion and extraction, or the reversibility. Ultimately they are useful in the determination of the diffusion coefficient, when making use of Equation13. If the redox is surface sensitive, the kinetics will be influenced by the surface functionalities, whereas if the redox is bulk sensitive, then the rate is limited by the diffusion process.

Any variation from reversible behavior for a redox process is demonstrated through variations in E_p and I. Reversibility requires that electron transfer kinetics are fast enough to maintain the concentrations of the oxidized and reduced species at a ratio sufficient to stabilize the electron transfer. If the electron transfer rate is small compared to the scan rate, the desired concentrations will not be maintained and the reaction process will be deemed *quasi*-reversible. The peak separation E_p provides information on the reversibility. For a reversible process $E_p = 59.2mV/n$, where n is the number of electrons transfered per molecule, and can be improved upon variation of scan rate. The irreversibility can also be indicated by the current ratio I_{pa}/I_{pc}, the ratio of the extracted current upon reduction compared to oxidation. The ratio is often less than unity as only a fraction of the molecules that were reduced on the forward scan are available for re-oxidation on the reverse scan, however the closer to a value of 1, the reaction is said to be more reversible.

Determination of I_{pa} and I_{pc} can be determined directly from the cyclic voltammogram. The peak height and baseline values for each oxidation and reduction are deduced, and the difference provides an estimate on the current value. The diffusion constant can be determined directly from the Randles-Sevcik equation (Equation 13), once the electrode area, ion concentration, scan rate, and peak currents are known. Holding electrode and electrolyte concentration constant, and plotting peak current I *vs* scan rate $\sqrt{v}$, a linear relationship should be observed where the diffusion constant is propertional to the slope. The diffusion constant for a series of electrolytes was determined, and is summarized in Table6. The cyclic voltammograms used to determine the diffusion coefficient can be found in the Appendix.

It should be noted that any experiment performed with chloride as an anion proved to be unsuccessful, regardless of concentration, voltage window, and scan rate. Reaction progress was hindered as the aluminum mesh quickly degrades in solution as demonstrated in Figure20. Voltammograms for such cases have been reported in the Appendix Figure43.

Table 6: Diffusion coefficient estimate using cyclic voltammogram technique and the Randles-Sevcik equation (Equation 13).

Salt	Diffusion Coefficient $[mol/L]$
KNO_3	0.0473
$Zn(NO_3)_2$	0.000182
AlN_3O_9	0.000539
$MgSO_4$	0.00207

Figure 20: Corrosion of aluminum mesh in potassium chloride solution.

Referring to Table5, it is possible to notice two recurring trends among each salt. In general, decreasing the scan rate and increasing the salt concentration both have have an increasing effect on the reversibility, as the potential difference between redox peaks decreases. As mentioned previously, the peak separation E_p provides information on the reversibility. Since peak separation is greatly effected by a change in scan rate, it can be said the reactions are diffusion limited. Figure21 demonstrates how decreasing scan rate increases the reversibility,

The diffusion flux is influenced by the concentration gradient near the electrode. The concentration gradient, in turn, is affected by the concentration of species at the electrode. Therefore, reactions which are diffusion-limited rely heavily on a high concentration of species at the electrode. Figures22 and 23 demonstrate trends to that effect.

Figure24 demonstrates the effect of changing the cation in solution while scan rate, concentration, voltage window, and anion remain constant. It can be seen that the $TiFe(CN)_6$ material is versatile and is able to accommodate a variety of ions, ranging from the monovalent Na^+ and K^+, divalent Zn^{2+}, and trivalent Al^{3+}. Ions are able to be reversibly inserted and extracted, and

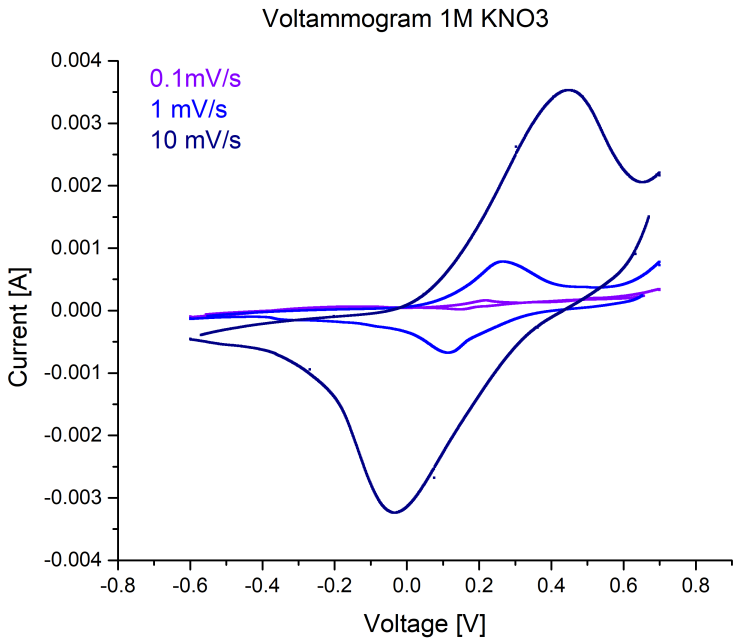

Figure 21: KNO_3 voltammograms taken at varying scan rates with constant electrolyte concentration. Note the increase in reversibility with a decrease in scan rate.

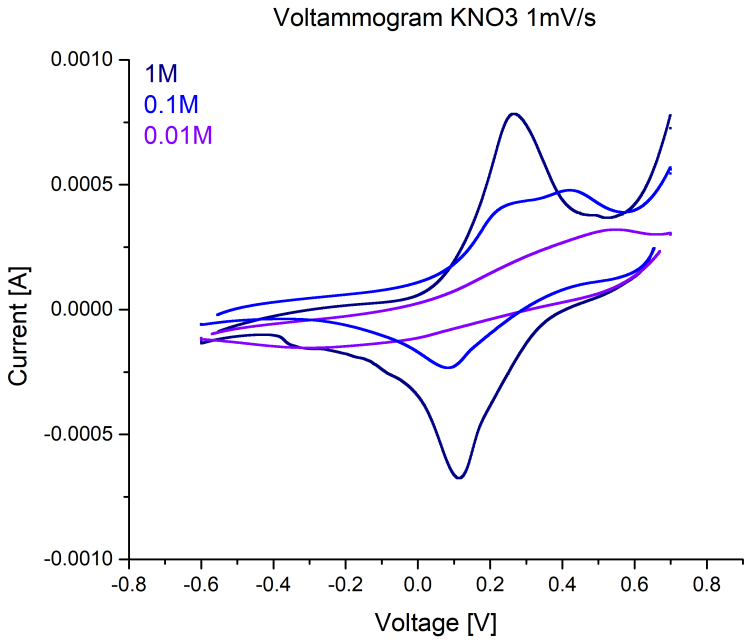

Figure 22: KNO_3 voltammograms taken at varying electrolyte concentration. Note how an increase in concentration leads to an increase in reversibility

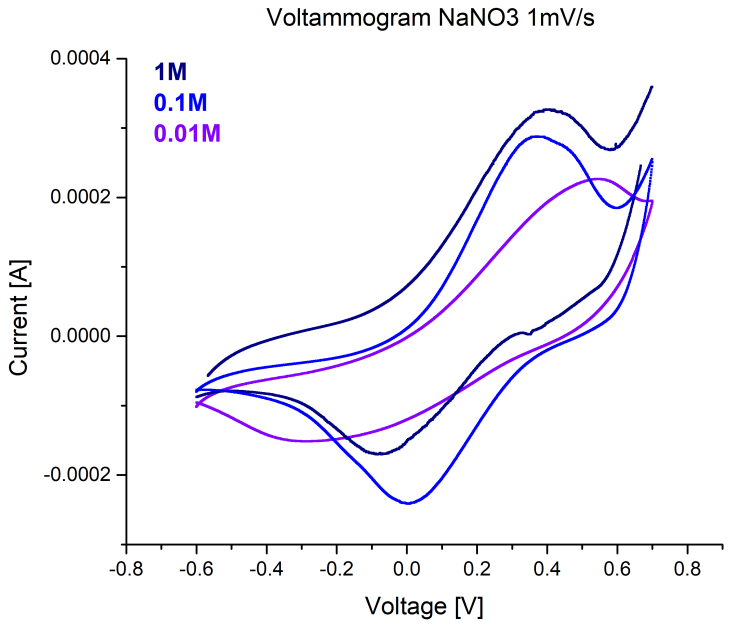

Figure 23: $NaNO_3$ voltammograms taken at varying electrolyte concentration. Note how an increase in concentration leads to an increase in reversibility

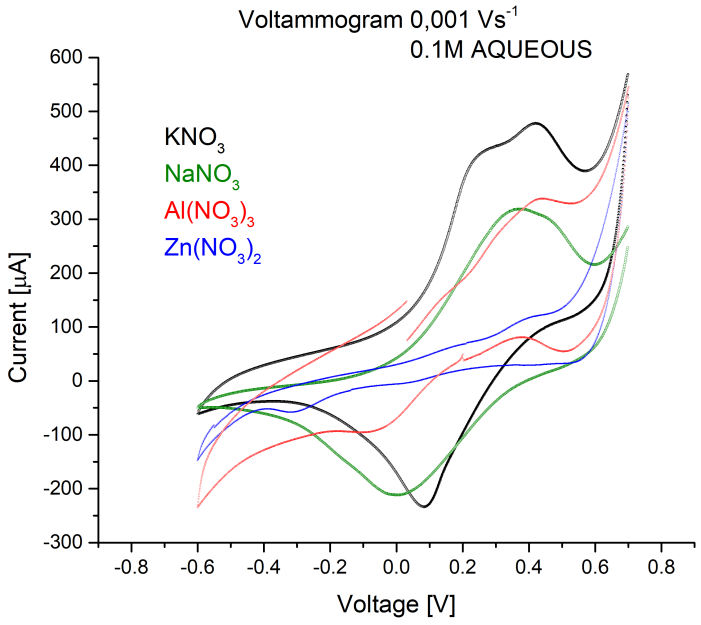

Figure 24: Cyclic voltammogram comparing different electrolyte solutions at a constant scan rate of $1mVs^{-1}$, and at a concentration of $0,1M$.

they are done so through a single or multi-step process. In the case of potassium, the extraction takes places at two different potentials, which is demonstrated by the presence of two peaks in the

oxidation. However, if the concentration of potassium is increased, the process seems to occur at a single potential (c.f. Figure22). In the case of sodium, the peaks are quite broad regardless of change in concentration (c.f. Figure23). This may be due to the presence of a multi-step extraction occurring at different sites. For Aluminum and Zinc, there are many distinguishable extraction and insertion processes occurring at different potentials. The insertion and extraction processes may demonstrate a larger variation as they may be dependent on ion size as well as ion charge. The cyclic voltammograms demonstrate that both KNO_3 and $NaNO_3$ are likely more promising than the alternative electrolytes. Not only do they possess quality life cycle, but they also show to be relatively reversible and show high capacities (proportional to the area beneath the voltammogram normalized by the number of exchanged electrons, n).

For hexacyanoferrates in this potential window, it is commonly reported that the active metal is iron. Potassium and sodium have shown to be the most appealing cations and an optimal concentration has been selected. In order to further explore the electrochemical properties of the material, it is necessary to explore variations in the voltage range. However, in order to obtain higher electrochemical performances, we decided to facilitate the diffusion processes. Therefore, we optimized both electrode thickness and mass, and decided to work with relatively low mass loadings and rather thin films. By decreasing the active material percentage to 50%, the carbon content was been increased, and a higher conductivity of the formulated electrode was been achieved.

Figure25 shows a cyclic voltammogram ranging from -1.3V to +1.3V with sodium and potassium nitrate. As we have seen there is the reversible process taking place from 0V to 0.5V, as well there is what seems to be a reversible process occurring at the higher end of the potential range. What is peculiar in this process is the presence of an irreversible redox pair at lower potentials. A reduction occurs at a potential of -1.3V, however there is no associated oxidation upon charge. In order to maximize efficiency a lower limit will need to be applied to the cycle, selected at -0.7V. Figure26 depicts the associated cyclic voltammogram in the optimized conditions, conducted at a slow scan rate of 5mVs^{-1} in an attempt to acquire high resolution redox processes.

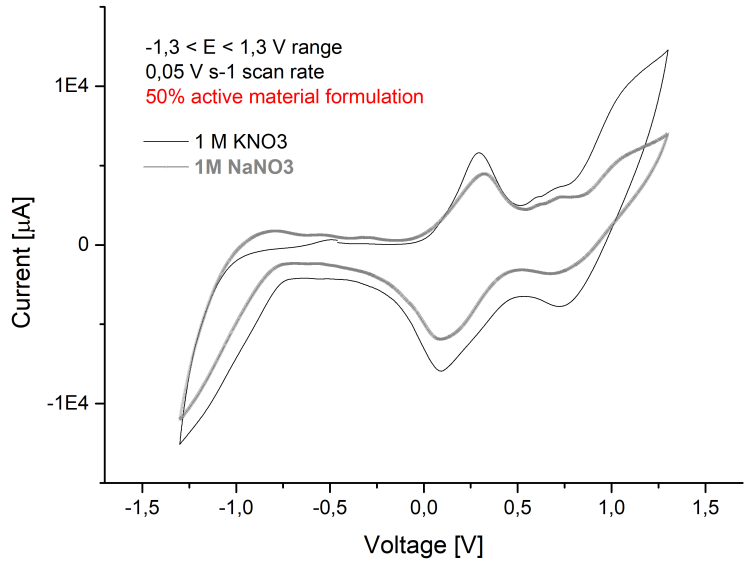

Figure 25: A voltage window ranging from -1.3V to +1.3V *vs* SCE with sodium and potassium nitrate.

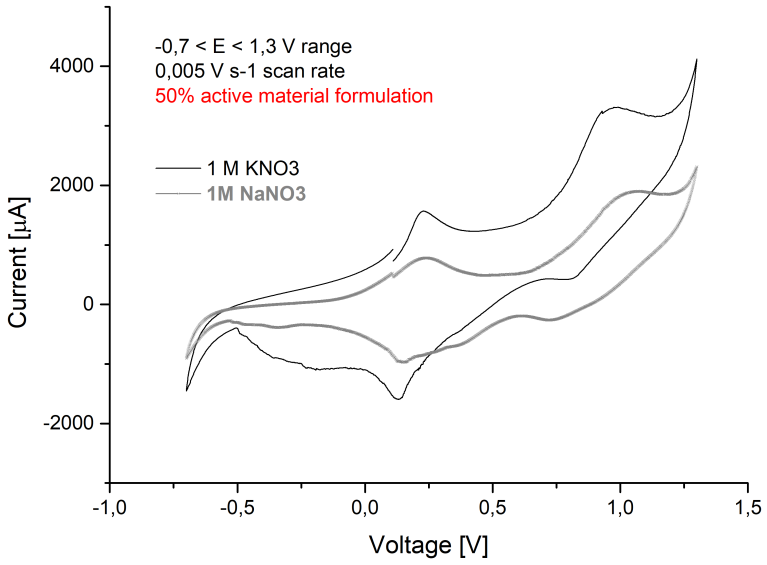

Figure 26: A voltage window ranging from -0.6V to +1.3V *vs* SCE with sodium and potassium nitrate.

5.4 Galvanostatic Cycling

Galvanostatic Cycling with Potential Limitation (GCPL) is a common technique dedicated to battery testing. A constant current is imposed and therefore the battery cycles under galvanostatic mode. potential window can be set in order to limit the potential decrease during discharge (reduction) and increase during charge (oxidation). The material has been tested as positive electrode in organic electrolyte, by using a coin cell assembly. To do so the electrochemical response against Li/Li+ couple (negative electrode) has been registered. The cathode contains 50% of active material (cathode), 20% of carbon black, 20% of carbon fibers, and 10% of PTFE. The constituents were mixed in an agate mortar, so that thin films were obtained and properly cut and successively used to assemble the coin cell. Speaking of electrochemical performances, they could vary based on the electrode thickness and electrode mass. For this reason, test cells can be performed with different mass loads. We decided to work with relatively mass loadings and rather thin films, in order to facilitate diffusion processes. A typical electrode has an active material mass loading of 2.5 mg/cm2. Moreover, even changing the percentage of the electrode constituents may help in getting cycling improvements. For instance, a higher conductivity may be achieved by increasing the carbon content. A further factor that plays an important role is the current rate, i.e. the imposed current. It is generally calculated from the theoretical capacity, dividing it by a chosen factor. Lets take an example: if one mole of Li per mole of AM should enter the structure in 20 h, the theoretical capacity (in mAh) should be divided by 20 h to get the current (mA) that allows the desired insertion rate. In this case we refer to C/20 rate, a typical value. Using this notation, a current rate of C/40 would be twice slower, while 5C would insert 5 moles of Li per mole of AM in just one hour. A material that can be cycled both at low and high currents with little capacity fade is an excellent material. Commonly, at high current rates the capacity is lower and the battery is able to insert and extract less ions, as proven by some made tests.

Coin cells, Figure27 consist in stacked layers: two cases enclose the electrodes, separated by the electrolyte solution. After having been stacked, coin cells are closed by means of a mechanical machine. Formally, the cell may be described as simply as: AM/1M LiPF6/EC:DEC//EC:DEC/Li (EC:DEC as a common used organic solvent mixture and stands for ethylene carbonate: diethyl carbonate).

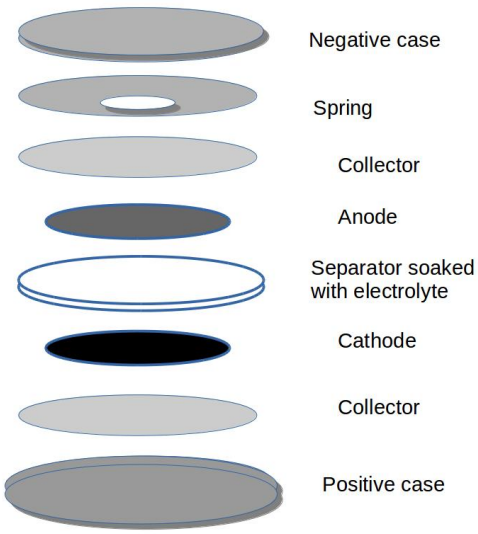

Figure 27: Typical set-up for a coin cell.

Figure28 shows the potential variation as a function of time when a current density of 86 A/mg is imposed to coin cell A (c.f. Table7) which corresponds to a rate of 1C.

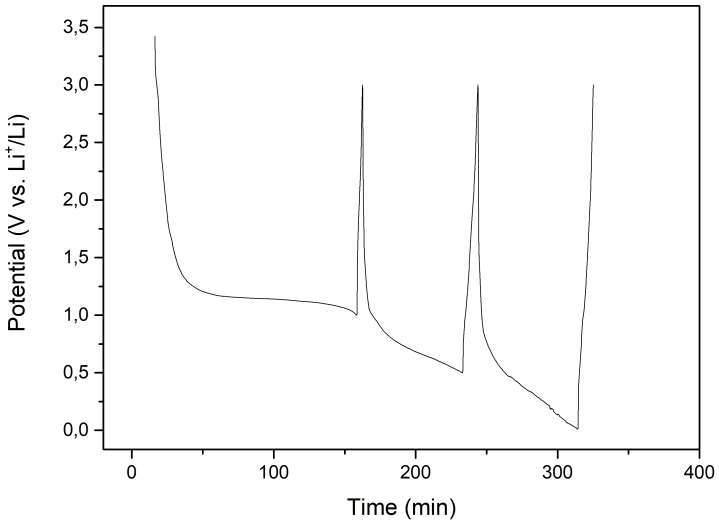

Figure 28: Galvanostatic cycling of a cell in the 0.01-0.03V potential range. Note the large insertion at 1.1-1.2V, and the lack of extraction during charge.

The response can be attributed to the cathode only (positive electrode, our material) since the anodic compartment (negative electrode, Li metal) should not act as the limiting process. Different voltage windows have been used in this first test. Starting from an OCP value of 3.3 V,

a negative current of -30 A is first imposed, forcing the reduction of the active material up to a potential of 1.0 V *vs* Li+/Li. The material is able to insert a well-defined amount of lithium in the structure (for about 150 minutes), and this insertion takes place around 1.2 V *vs* Li/Li+. This capacity is found to be irreversible as the first charge is limited to few minutes only. Even though a positive current of 30A is applied back to 3.0 V, the inserted lithium is not able to exit the lattice. By lowering the potential to 0.5 V and 0.01 V, the amount of inserted lithium is less without any beneficial response in the subsequent anodic scan: the inserted lithium cannot be released after inversion of the electrode polarity. All in all, even though the proposed material is capable to insert lithium at relatively low potential, and this makes the electrode suitable for an anode, its kinetic response is clearly irreversible.

Table 7: Characteristics and operating conditions of two cycled coin cells.

Coin Cell	Electrode Mass (mg)	AM mass (μg)	Current (μA)	Current density (μAmg^{-1})	C rate	Potential Range (V)
A	0.7	0.35	30	86	1C	0.01-3.0
B	0.6	0.30	26	87	1C	2.8-4.2

Another test was done on a fresh coin cell, but on positive direction first (charge) on an extended range of potential, $1.0 \leq E \leq 4.2$ V *vs* Li+/Li. The response suggested a possible use of the synthesized material as a cathode, and further investigations have been made in a reduced potential window to achieve high reversibility (Cell B, cf. Table T1). Figure x2 displays a set of charge and discharge curves of this coin cell in the range $2.8 \leq E \leq 4.2$ V *vs* Li+/Li. Surprisingly, this test demonstrated that the material was able to perform a series of discharge/charge processes, with the first cycle displaying a lower capacity than the 100th. The plateau at which the lithium is inserted and successfully released is at about 3.6-3.8 V *vs* Li/Li+, a value very high which with no doubt can be used as cathode. The delivered capacity is 35 mAh/g.

As seen in Figure30, coin cell B does not only display a decreasing capacity but also presents an efficiency of 100% in the range of potential the explored, that is 2.8-4.2 V. Eventually, even though the proposed active material was meant to be used as anode, the electrochemical traces reported in organic electrolytes suggests it should be used as a cathode. The delivered capacity is relatively low (35 mAh/g) but at an interesting high potential of 3.6 V, paving the way for future study on high power batteries.

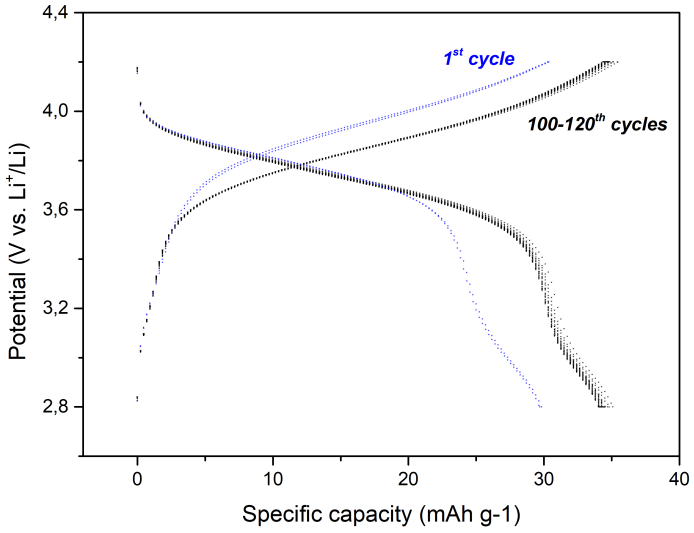

Figure 29: . Electrochemical curves of cycled coin cell B in the 2.8 4.2 V potential range. A high reversibility is achieved in this region and a specific capacity of 35 mAh/g is obtained.

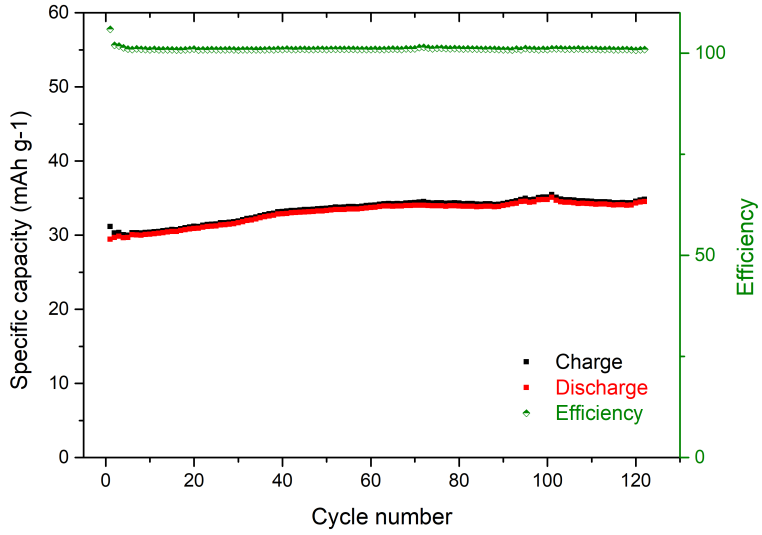

Figure 30: Cyclability of coin cell B. Both specific capacity in charge and discharge and efficiency are displayed in relation to the number of cycles. .

6 Conclusion

Research based on secondary cells is constantly developing due to its importance in technological applications. Cells with an excellent cyclability are sought out, and performances can be improved by changing operative conditions as well as the materials: new electrodic materials are tested, especially those characterized by an open-framework structure, which allows for rapid insertion and extraction with little lattice strain. Different electrolytes and solvents are used in order to achieve desirable ion-mobility and stability within a given the potential window.

In the present work, a study on Titanium Hexacyanoferrate Prussian blue analogue has been achieved. According to the literature, this may be a compound capable to function at relatively low potentials, perhaps even as an anodic material. For this reason, we attempt to provide electrochemical information on the material in both aqueous and organic electrolytes. Synthesis was carried out via precipitation method. Characterization revealed the crystallinity of the compound and cubic symmetric structure, in particular a $Pm\overline{3}m$ space group with cell parameter a = 10.190(2) $\mathring{A}$. The combination of TGA and ICP-OES provided useful in assigning the chemical formula to the synthesized material: $Ti_{1.3}FeCN_6 \cdot 1.8H_2O$.

Cyclic voltammetry has been used to study the electrochemical behavior of the PTFE-formulated electrodes in aqueous solutions. A deep and systematic study on the material has been done, by varying operating potential window, scan rate, salt composition, and salt concentration. Potassium and sodium nitrates show the best response in terms of redox reversibility, diffusion coefficient, and cycle life of the electrode. In order to obtain higher electrochemical performances, we decided to facilitate diffusion processes. Therefore we optimized both electrode thickness and mass, and decided to work with relatively low mass loadings and thin films. By decreasing the active material percentage to 50%, the carbon content was increased, and a higher conductivity of the formulated electrode was achieved. As a consequence of electrolyte nature, salt concentration, and general electrode optimization, we were finally able to cycle the material in a wide voltage range. Higher capacities were obtained, demonstrating greater performances in aqueous medium. No reversible redox process occurred at lower voltages, as the material seems more suited to act as a cathode.

The material was further tested as cathode in organic electrolyte, by making use of a coin cell assembly with Li metal foil as anode. By means of galvanostatic cycling, it was possible to obtain the capacity and efficiency of the battery prototype, and investigate the electrochemical behaviour of titanium hexacyanoferrate in an organic medium. First, we explored low potential windows down to 0.01 V *vs* Li^+/Li and the capabilities of the material as anode. The inserted lithium was not able to be released after inversion of the electrode polarity even though the proposed material was able to insert lithium at relatively low potentials (1.1-1.2 V), its kinetic response is clearly irreversible. Secondly, upper potentials were investigated, ranging from 2.8-4.2 V *vs* Li^+/Li. We demonstrated that the material was able to perform a series of discharge/charge processes, with the first cycle displaying a lower capacity than the 100th. The plateau at which the lithium is inserted and successfully released is at about 3.6-3.8 V. vs. Li^+/Li, a value very high which with no doubt can be used as cathode. The delivered capacity is relatively low (35 mAh/g) but at an high potential, paving the way for future study on high power batteries.

References

[1] Li, Wei-Jie, Investigation on the promising electrode materials for rechargeable sodium ion batteries (Doctoral Dissertation), Institute for Superconducting and Electronic Materials, University of Wollongong, Australia 2015. http://ro.uow.edu.au/theses/4603

[2] Chen, Haisheng, et. al., Progress in Electrical Energy storage System: A Critical Review. Elsevier, Progress in Natural Science 19 (2009): 291-312.

[3] Colin, V., Scrosati, B. Modern Batteries, 1997.

[4] Asahi Kasei Company, Taiyou Research. Global Market for Lithium-Ion Batteries – Forecast, Trends and Opportunities 2014-2020, Tokyo Japan (2014).

[5] Guduru, R. K., Icaza, J. C., A Brief Review on Multivalent Intercalation Batteries with Aqueous Electrolytes. Nanomaterials, 2016, 6, 41. doi:10.3390/nano6030041

[6] Yabuuchi, N., et al., Research Development on Sodium-Ion Batteries. Chem. Rev. 2014, 114, 11636-11682.

[7] Kim, H., et al., Aqueous Rechargeable Li and Na Ion Batteries. Chem. Rev. 2014, 114, 11788-11827.

[8] Wang, Y., et al., Emerging Non-Lithium Ion Batteries. Elsevier, Energy Storage Materials 4, 2016, 103-129.

[9] Lapidus, S. H., et al., Solvation Structures and Energetics of Electrolytes for Multivalent Energy Storage. Phys. chem. 2014, 16, 21941-21945.

[10] Liu, M., Spinel Compounds as multivalent battery cathodes: A Systematic evaluation based on *ab initio* Calculations. Energy Environ. Sci. 2015, 8, 964-974.

[11] Ma F., et al., Energy Storage Materials Derived From Prussian Blue Analogues. Elsevier. Science Bulletin, 2017, http://dx.doi.org/10.1016/j.scib.2017.01.030

[12] Nie, P., et al., Flexible Metal-organic Frameworks as Superior Cathodes for Rechargeable Sodium-ion Batteries. Journal of Materials Chemistry A. 2013. DOI: 10.1039/C5TA03197D

[13] Sun, X., et al., A New Gridding Cyanoferrate Anode Material for Lithium and Sodium Ion Batteries: TiFe[Fe(CN)6] with excellent Electrochemical Properties, Elsevier Journal of Power Sources 314, 2016, p. 35-38.

[14] Wang J., Analytical Electrochemistry, Sec. ed. Wiley-VCH, 2000.

[15] Brett C. M. A., Brett A. M. O., Electrochemistry Principles, Methods, and Applications, Oxford Science Publications, 1993.

[16] Lledo-Fernandez Electro-Catalytic Reactions (Doctoral Dissertation), University of Hull, 2009.

[17] Protti, P. Introduction to Modern Voltammetry and Polarographic Analysis Techniques, Fourth ed., Amel Electrochemistry, 2001.

[18] Compton, R. G., Banks, C. E., Understanding Voltammetry, Second ed., Imperial College Press, 2011.

[19] Kissinger P. T., Heinman, W. R., Cyclic Voltammetry, J. Chem. Educ., 1983, 60(9), p.702.

[20] Aurbach, D., Nonaqueous Electrochemistry, First Ed., CRG, 1999.

[21] Dahn, J. R., et al., Rechargeable Lithium Batteries with Aqueous Electrolytes. Science, 1994, 20, p. 1115-1118

[22] Kundu, D., et. al., the Emerging Chemistry of Sodium Ion Batteries for Electrochemical Energy Storage, Angewandte Chemie International Ed., 150. 2015.

[23] Gregory, T.D., Nonaqueous Electrochemistry of Magnesium. J. Electrochem. Soc. 1990, 137, 775-780.

[24] Novak, P., et al., Electrochemical Insertion of Magnesium in Metal Oxides and Sulfides from Aprotic Electrolyties. J. Electrochem. Soc. 1993, 140, 140-144.

[25] Liu, S., et. al., Copper Hexacyanoferrate Nanoparticles as Cathode Material for Aqueous Al-ion Batteries, J. Mater. Chem. A., 2015, 3: pg959.

[26] Liu, S., et al., Aluminium Storage behavior of Anatase TiO_2 Nanotube Arrays in Aqueous Solution for Aluminium Ion Batteries. Energy Environ. Sci., 2012, 5, p. 9743-9746.

[27] He Y. J. et al., Black Mesoporous Anatase TiO_2 nano leaves: A high Capacity and high rate anode for aqueous Al-ion batteries. J. Mater. Chem. A 2014, 2, p.1721-1731.

[28] Cui, Y., et al., Reversible Multivalent (Monovalent, Divalent, Trivalent) Ion Insertion in Open Framework Materials. Adv. Energy. Mater., 2015, 5, p.1-10.

[29] Gupta, T., Improving the cycle life of a high-rate, high potential aqueous dual-ion battery using hyper-dentritic zinc and copper hexacyanoferrate. J. Power Sources, 2016, 305, p.22-29.

[30] Xu, C., et al., Energetic Zinc Ion Chemistry: The Rechargeable Zinc Ion Battery. Angew. Chem., 2012, 51, p. 933-937.

[31] Yuan, C. et al., Investigation of the Intercalation of the Polyvalent Magnesium and Zinc Cations into gamma-MnO2 for rechargeable aqueous battery. Electrochim. Acta., 2014, 116, p.404-412.

[32] Jia, Z. et al., Copper Hexacyanoferrate with a Well-defined Open Framework as a Positive Electrode for Aqueous Zinc Ion Batteries. Mater. Chem. Phys., 2015, p. 149-150,601-606.

[33] Eftekhari, A., Potassium Secondary Cell based on Prussian Blue Cathode, J. Power Sources, 2004, 126, p.221-228.

[34] Eftekhari, A., et al., Potassium Secondary Batteries, Amer. Chem. Soc. Applied Materials and Interfaces, 2016. DOI: 10.1021/acsami.6b07989

[35] Minato, The Influence of Graphitic Structure of Carbon Electrode on Aging Behavior of Electric Double Layer Capacitor. Electrochemistry, 2012.

[36] Aparicio, C., et al., Thermal Decomposition of Prussian Blue Under Inert Atmosphere, J.

Therm. Anal Calorim, 2012, 110: pg661-669. DOI 10.1007/s10973-011-1890-1

[37] Cosgrove, J. G., et. al., Preparation of Ferrous Ferricyanide (Not Turnbull's Blue), J. Am. Soc., 1973, 95: pg1083-1086.

[38] Lejeune, J., et. al., Applocation of the Infrared Spectroscopy to the structural study of Prussian blue analogues, Comptes Rendus Chimie, 2014, 17: pg534-540.

Appendix

The following figures were used to determine the diffusion coefficient of $Zn(NO_3)_2x6H_2O$, KNO_3, $AlN_3O_9x9H_2O$, and $MgSO_4$. Values reported in the results section, Table6.

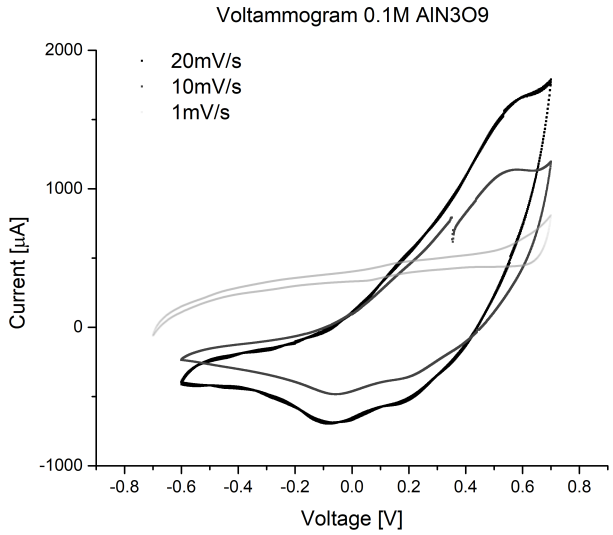

Figure 31: AlN_3O_9 voltammograms taken at varying scan rates. The electrolyte concetration remains constant throughout rate variation.

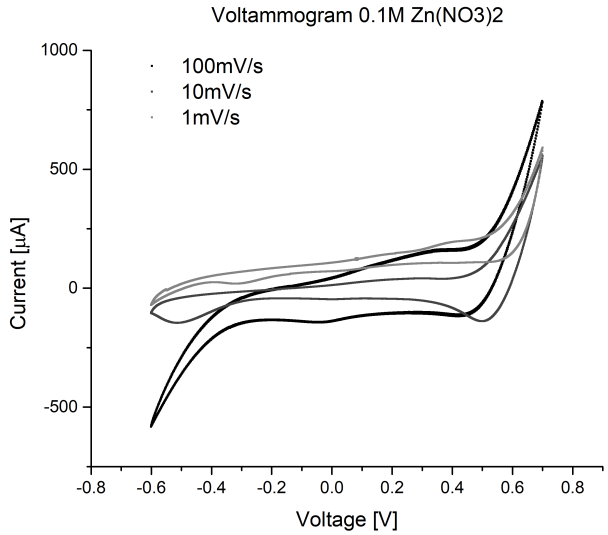

Figure 32: $Zn(NO_3)_2$ voltammograms taken at varying scan rates with constant electrolyte concentration.

Several samples of voltammograms recorded throughout experimentation.

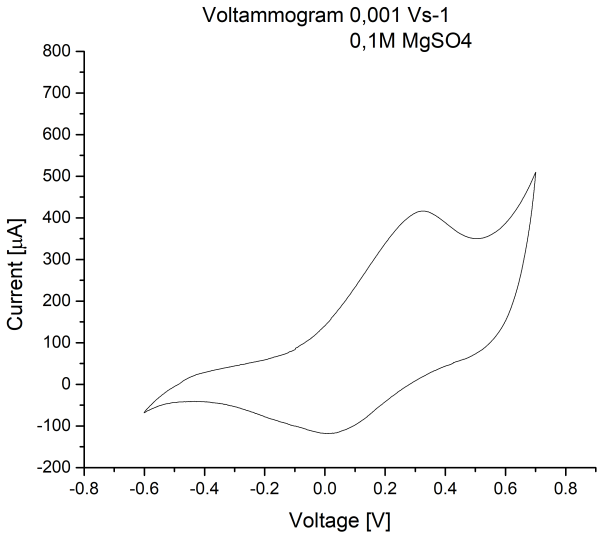

Figure 33: CV voltammogram of $MgSO_4$ performed at 1mVs-1 at a concentration of 0,1M. Peaks occur at 0.01395V and 0.31295V.

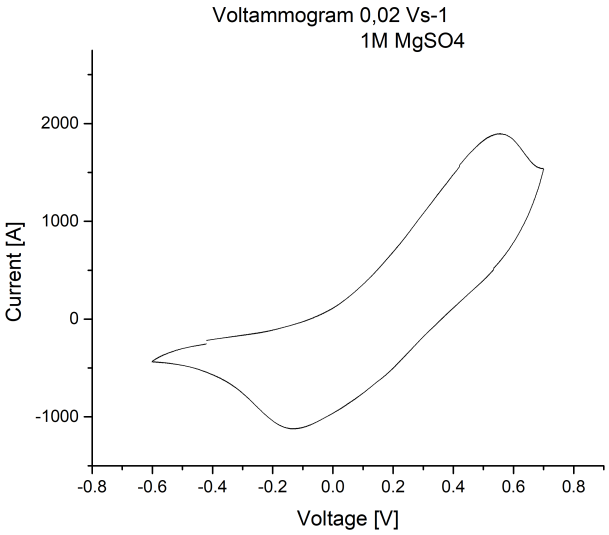

Figure 34: CV voltammogram of $MgSO_4$ performed at 20mVs-1 at a concentration of 1M. This experiment has both a higher scan rate and concentration than the previous $MgSO_4$ voltammogram, the peaks occur at -0.12163V and 0.55114V.

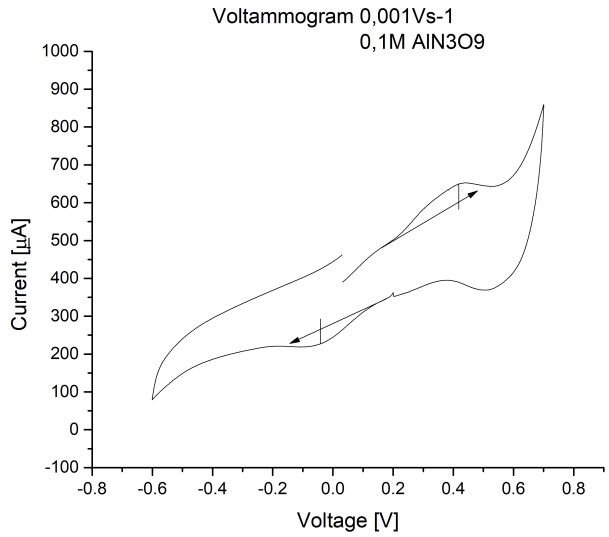

Figure 35: CV voltammogram of AlN_3O_9 performed at 1mVs-1 at a concentration of 0,1M. Peaks occur at -0.04126V and 0.41865V.

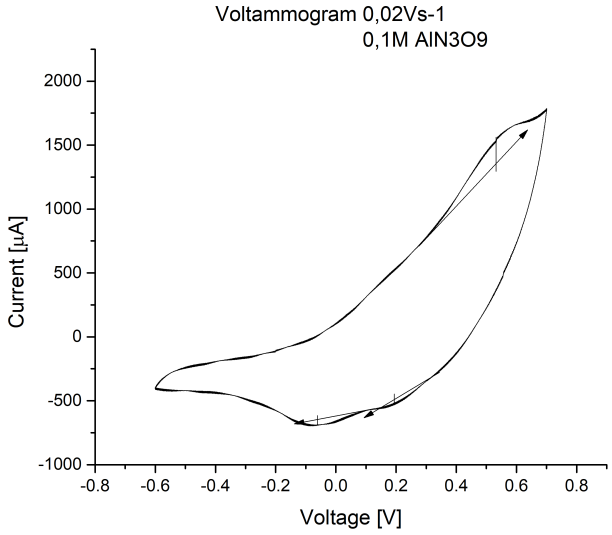

Figure 36: CV voltammogram of AlN_3O_9 performed at 20mVs-1 at a concentration of 0,1M. Peaks occur at -0.06205V and 0.53279V.Note the development of a new peak occuring at 0.2V the reduction process.

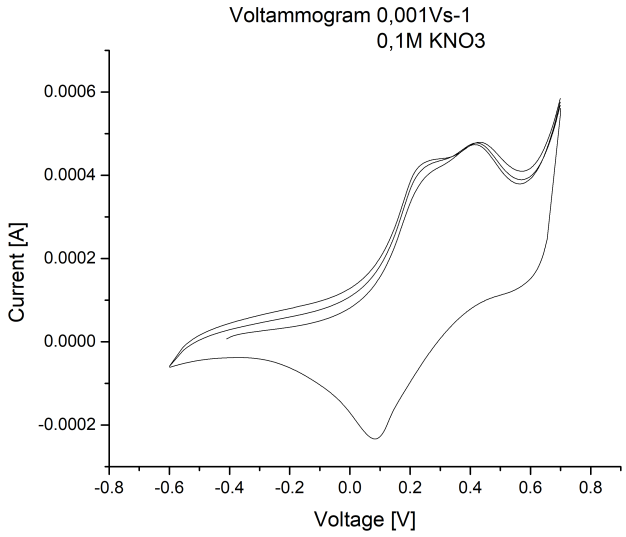

Figure 37: CV voltammogram of KNO_3 performed at 1mVs-1 at a concentration of 0,1M. Peaks occur at -0.0869V and 0.26509V.

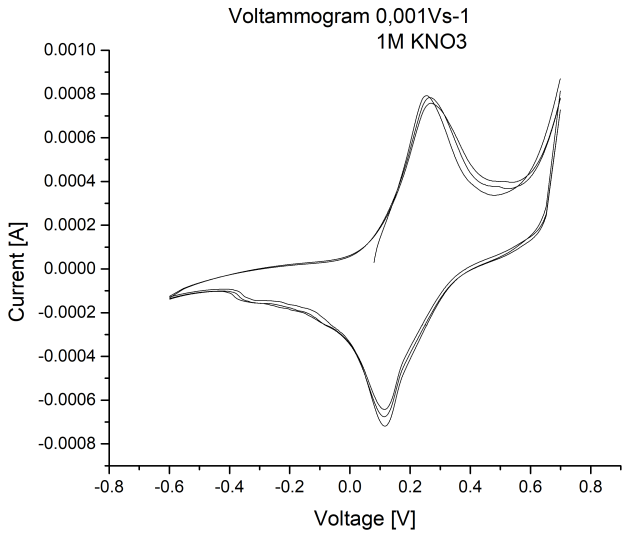

Figure 38: CV voltammogram of KNO_3 performed at 1mVs-1 at a concentration of 1M. Peaks occur at 0.1170V and 0.26613V. The reaction at higher concentration becomes more reversible.

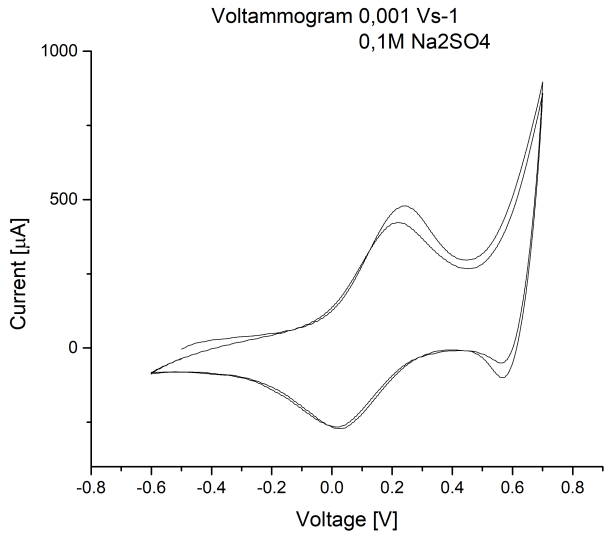

Figure 39: CV voltammogram of Na_2SO_4 performed at 1mVs-1 at a concentration of 0,1M. The peaks occur at 0.01601V and 0.21951V. Experiments performed with this salt at different concentrations and scan rates did not yield any successful results.

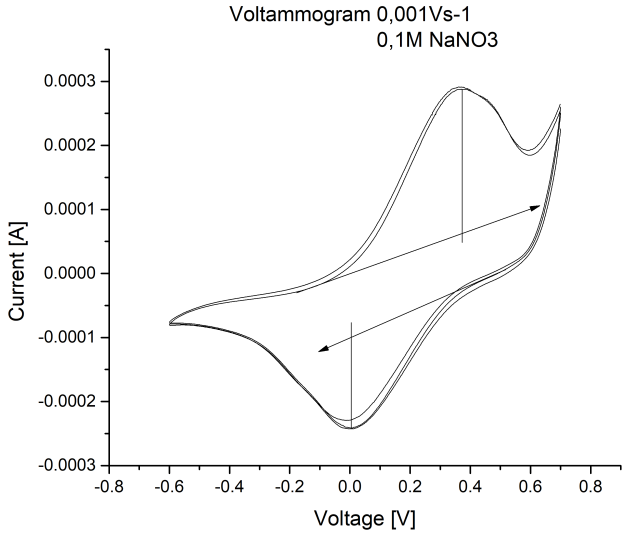

Figure 40: Sample CV voltammogram of $NaNO_3$ performed at 1mVs-1 at a concentration of 0,1M. The peaks occur at 0.00515V and 0.37308V.

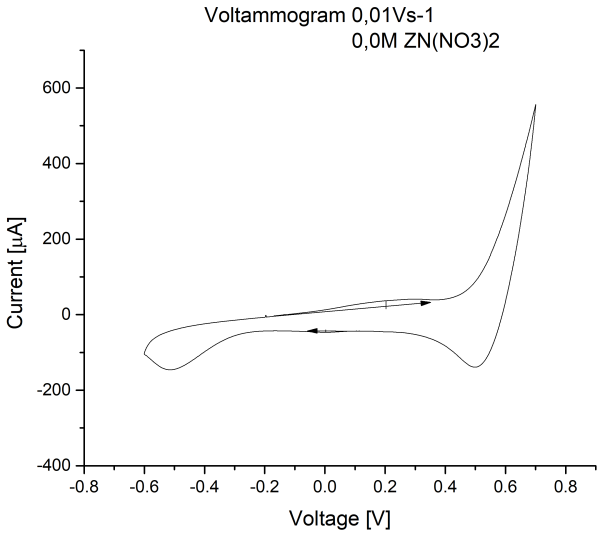

Figure 41: Sample CV voltammogram of $Zn(NO_3)_2$ performed at 10mVs-1 at a concentration of 0,1M. The peaks occur at 0.00204V and 0.20007V.

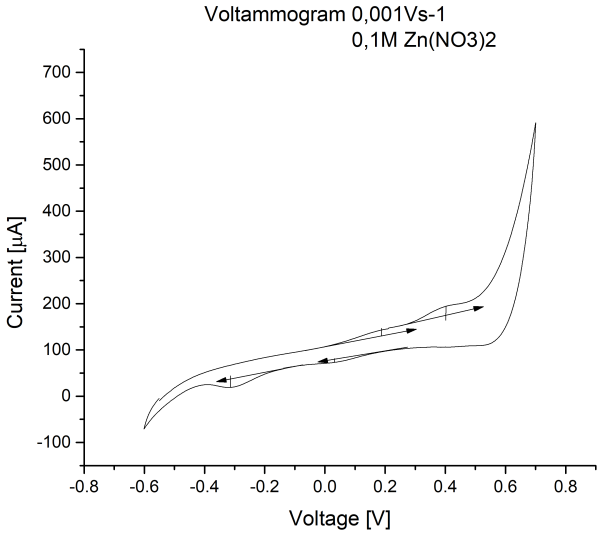

Figure 42: Sample CV voltammogram of $Zn(NO_3)_2$ performed at 1mVs-1 at a concentration of 0,1M. With the slower scan rate two sets of peaks appear, with potentials of 0.14025V and 0.49853V, and at -0.31375V 0.19214V.

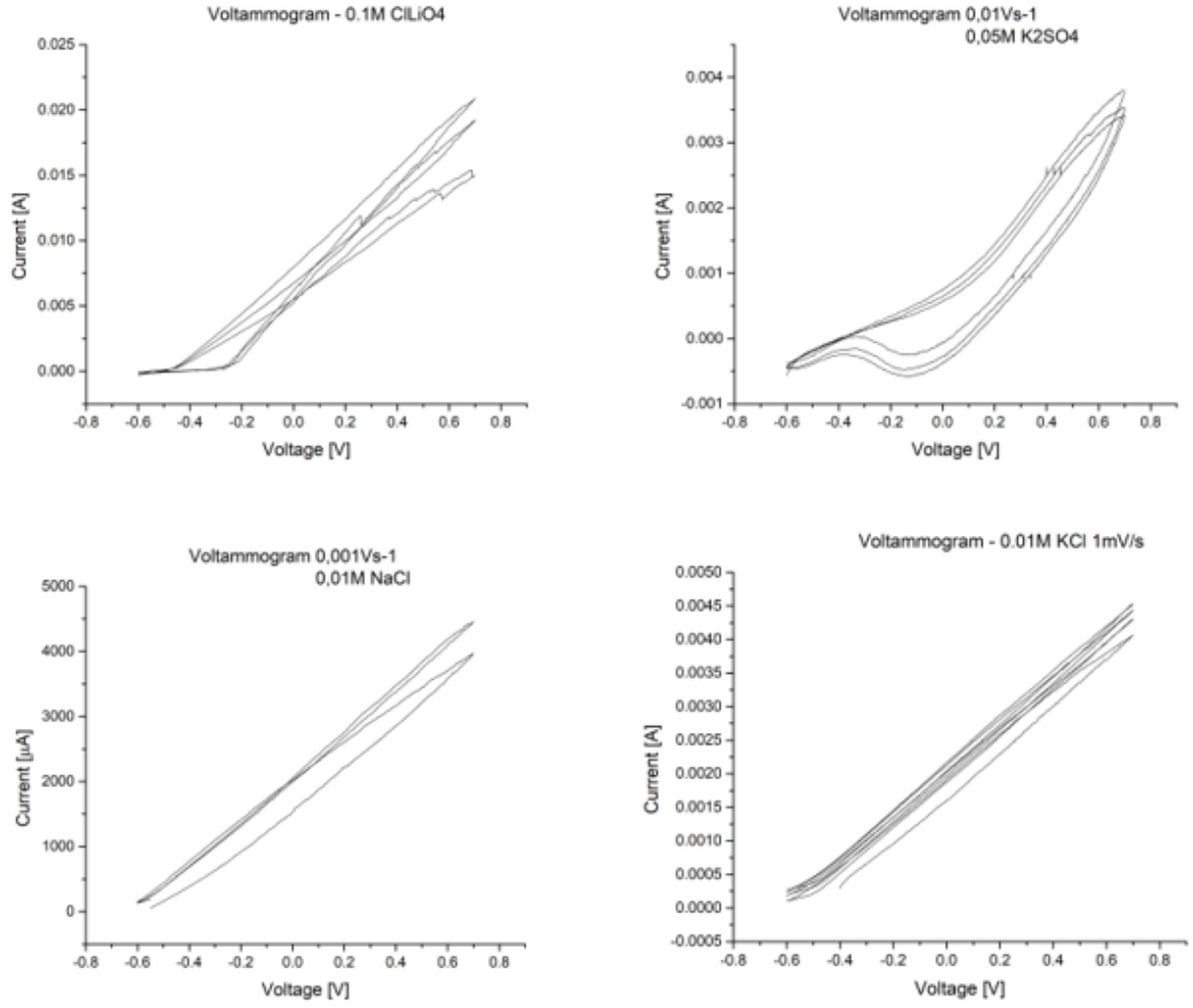

Figure 43: Set of samples analyzed via cyclic voltammetry. Each of the four salts $ClLiO_4$, KCl, $NaCl$, and K_2SO_4 did not demonstrate the properties of a reversible redox reaction. The CV diagrams displayed were selected as the "best" from each sample.